RESEARCH ARTICLE SUMMARY

NEUROSCIENCE

# Dual-polarity voltage imaging of the concurrent dynamics of multiple neuron types

**Madhuvanthi Kannan*†, Ganesh Vasan*†, Simon Haziza†, Cheng Huang, Radosław Chrapkiewicz, Junjie Luo, Jessica A. Cardin, Mark J. Schnitzer*, Vincent A. Pieribone***

**INTRODUCTION:** Signal processing in the brain involves the concerted dynamics of multiple distinct cell subtypes that belong to excitatory and inhibitory neuron populations. To uncover how they synergize their activities in real time, it is important to record the voltage dynamics of multiple identified subtypes simultaneously. Genetically encoded fluorescent voltage indicators (GEVIs) are ideally suited to reveal the millisecond-scale activation dynamics of one or more genetically identified neuron types in awake animals.

**RATIONALE:** We previously introduced the green and red fluorescence resonance energy transfer (FRET)–opsin GEVIs Ace-mNeon and VARNAM, which are fusion proteins of voltage- sensitive rhodopsin from *Acetabularia* with bright fluorescent proteins mNeonGreen and mRuby3, respectively. Ace-mNeon and VARNAM exhibit fluorescence decreases during voltage depolarization events such as action potentials (APs) and together constitute a pair of mutually compatible GEVIs that can be genetically targeted to two distinct neuron types for simultaneous dual-color voltage recordings. Using protein engineering and high-throughput voltage screening, we uncovered the second-generation GEVIs Ace-mNeon2 and VARNAM2, which have improved voltage sensitivities. We also identified the respective reverse response-polarity variants, pAce and pAceR, which exhibit fluorescence increases during APs. We reasoned that the four new indicators make up a suite of mutually compatible tools for multipopulation voltage recordings in behaving animals. When targeted to distinct neuron types, the indicators enable unambiguous cell-type identification from the voltage readout based on their fluorescence spectra, optical spike polarity, or both.

**RESULTS:** Our improved indicators exhibit enhanced voltage sensitivities to enable low-power (<25 mW $mm^{-2}$) recordings of spiking and transmembrane voltage dynamics from >50 individual neurons at a time in running mice and ~30-min continuous imaging in flies. Ace-mNeon2 voltage imaging from ~1200 neurons revealed visual cortical cell type–specific responses to behavioral-state transitions in awake mice. Cortical interneurons expressing somatostatin (SST) exhibited the most profound activation during a quiescence-to-arousal transition. Further, using simultaneous dual-polarity voltage recordings with Ace-mNeon2 and pAce, we examined the functional dynamics of pairs of neuron types. We unveiled a time-varying, state-dependent mutual antagonism in the voltage dynamics of SST- and vasoactive intestinal peptide (VIP)–expressing interneurons.

In the hippocampus, dual-polarity voltage imaging uncovered the differential contributions of distinct cell classes to the local field potential (LFP). Spiking in entorhinal cortex (EC)–projecting neurons, but not in SST interneurons, consistently phase-locked to the LFP. Moreover, using dual-color voltage imaging, we found that anterior cingulate cortex (ACC)– and EC-projecting excitatory subclasses differ in their responses to state change; the former uniformly increase their firing rates, but the latter do not.

Finally, by combining dual-polarity and dual-color imaging using three mutually compatible sensors from our suite, we extracted the simultaneous, real-time voltage dynamics of three neuron types. These subtypes belong to excitatory and inhibitory interneuronal subpopulations in the visual cortex and hippocampus of running mice.

**CONCLUSION:** Our work reveals functional correlations between targeted neuron types in visual cortical circuits during altered behavioral states as well as the contributions of distinct cell subclasses to hippocampal LFPs in running mice. Together, our findings benchmark multipopulation voltage imaging for investigations of the concerted dynamics of multiple cell classes in behaving animals. ■

The list of author affiliations is available in the full article online.
*Corresponding author. Email: mkannan@umn.edu (M.K.); gvasan@umn.edu (G.V.); mschnitz@stanford.edu (M.J.S.); vincent.pieribone@yale.edu (V.A.P.)
†These authors contributed equally to this work.
Cite this article as M. Kannan *et al.*, *Science* **378**, eabm8797 (2022). DOI: 10.1126/science.abm8797

READ THE FULL ARTICLE AT
https://doi.org/10.1126/science.abm8797

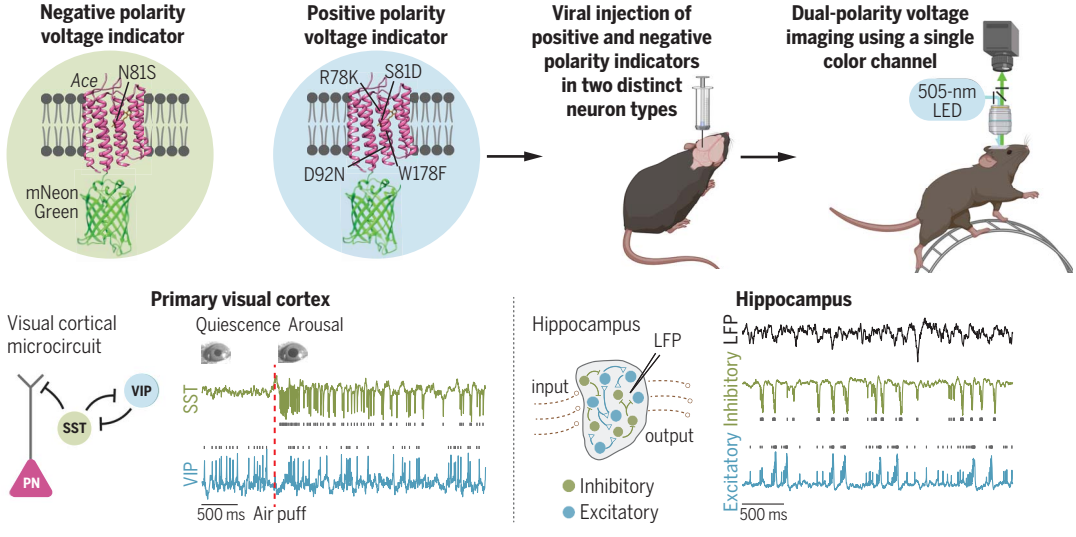


**Dual-polarity imaging of the simultaneous voltage dynamics of two neuron types in running mice.** Newly characterized negative- and positive-polarity GEVIs enable unambiguous identification of neuron types based on the optical spike polarity in single-color voltage imaging. Using this technique, we uncover a state-dependent antagonism between visual cortical SST and VIP interneurons as well as relative contributions to the LFP from hippocampal excitatory and inhibitory neurons. N81S, $Asn^{81}$→Ser; R78K, $Arg^{78}$→Lys; S81D, $Ser^{81}$→Asp; D92N, $Asp^{92}$→Asn; W178F, $Trp^{178}$→Phe; LED, light-emitting diode; PN, pyramidal neuron.

RESEARCH ARTICLE

NEUROSCIENCE

# Dual-polarity voltage imaging of the concurrent dynamics of multiple neuron types

Madhuvanthi Kannan[1,2]*†‡, Ganesh Vasan[1,2]*†‡, Simon Haziza[3,4]†, Cheng Huang[3], Radosław Chrapkiewicz[3,4], Junjie Luo[3,4,5], Jessica A. Cardin[6,7,8], Mark J. Schnitzer[3,4,5]*, Vincent A. Pieribone[1,2,6]*

Genetically encoded fluorescent voltage indicators are ideally suited to reveal the millisecond-scale interactions among and between targeted cell populations. However, current indicators lack the requisite sensitivity for in vivo multipopulation imaging. We describe next-generation green and red voltage sensors, Ace-mNeon2 and VARNAM2, and their reverse response-polarity variants pAce and pAceR. Our indicators enable 0.4- to 1-kilohertz voltage recordings from >50 spiking neurons per field of view in awake mice and ~30-minute continuous imaging in flies. Using dual-polarity multiplexed imaging, we uncovered brain state–dependent antagonism between neocortical somatostatin-expressing ($SST^+$) and vasoactive intestinal peptide–expressing ($VIP^+$) interneurons and contributions to hippocampal field potentials from cell ensembles with distinct axonal projections. By combining three mutually compatible indicators, we performed simultaneous triple-population imaging. These approaches will empower investigations of the dynamic interplay between neuronal subclasses at single-spike resolution.

The dynamic interplay of multiple excitatory and inhibitory neuronal subtypes is central to how the brain processes information. During motor or sensory processing, the external environment and an animal's internal state can affect the activity of neocortical interneurons, which in turn modulate excitatory projection neurons (*1*–*5*). Likewise, in the hippocampus, different ensembles of projection neurons exhibit state-dependent changes in spiking activity related to learning and memory (*6*–*9*). However, how different neural subclasses coordinate their dynamics in real time remains poorly understood, owing to an inability to measure the spiking activity of two or more genetically defined or projection-targeted neural ensembles simultaneously.

Genetically encoded voltage indicators (GEVIs) enable targeted recordings of spiking and subthreshold activity with submillisecond temporal precision (*10*–*12*). Although extensive protein engineering has spawned a host of new sensors (*13*–*24*), existing GEVIs are not optimized for concurrent, targeted recordings from two or more neuron types in behaving animals.

We previously introduced the green and red fluorescence resonance energy transfer (FRET)–opsin GEVIs Ace-mNeon and VARNAM (*17*, *18*). FRET-opsin GEVIs are fusions of a bright fluorescent protein (FP; the FRET donor) to a transmembrane opsin with a voltage-sensitive light absorption spectrum (the FRET acceptor) (*25*, *26*). This modular design enables voltage imaging in live animals with a high dynamic range of fluorescence signaling but at far-lower illumination levels (~25 mW $mm^{-2}$) than those (1 to 10 W $mm^{-2}$) required by opsin voltage indicators (*16*, *19*, *22*, *23*, *27*). Imaging studies using FRET-opsins have generally monitored the time-dependent emissions of the bright FRET donor but not those of the opsin FRET acceptor, because the latter's fluorescence is too dim to augment the detection of voltage signals. Thus, only one fluorescence channel is needed to image a FRET-opsin GEVI, with excitation and emission wavelength bandwidths matching those of the bright donor (*17*, *18*, *25*). Ace-mNeon and VARNAM comprise a fusion of the *Acetabularia* (Ace) rhodopsin (*17*, *18*) to the bright FP mNeonGreen (*28*) or mRuby3 (*29*), respectively. Notably, Ace-mNeon and VARNAM have demonstrated optical compatibility for concurrent recordings in live flies (*18*).

## Protein engineering of negative- and positive-polarity FRET-opsins

To improve the sensitivities of Ace-mNeon and VARNAM for recordings in awake mice, we performed protein engineering and high-throughput screening of voltage responsivity in excitable human embryonic kidney (HEK) cells (Fig. 1, A and B) (*18*, *30*, *31*). Our screening platform scores GEVIs for brightness, voltage sensitivity, and kinetics in a plate-based format, achieving a capacity of 120 unique variants per day with a sample content of ~2000 cells per variant (*18*).

In Ace-mNeon and VARNAM, depolarization-dependent quenching by Ace of fluorescence from the FP leads to depolarization-evoked fluorescence decreases as the readout of voltage changes. To improve voltage sensitivity, we sought to enhance the FRET transfer by optimizing the Ace-FP linker (*32*). In Ace-mNeon, we also performed site-saturation mutagenesis at Ace N81 ($Asn^{81}$) and screened a library of N81X positional mutants (where X is any amino acid) (Fig. 1A and fig. S1) (*18*). Screening of mutagenic libraries uncovered variants with increased response amplitudes (Fig. 1B and fig. S2). Ace-mNeon N81S G229Y ($Asn^{81}$→Ser and $Gly^{229}$→Tyr) and VARNAM Δ228W Δ229R G231I (deletion of $Trp^{228}$ and $Arg^{229}$, and $Gly^{231}$→Ile) (henceforth, Ace-mNeon2 and VARNAM2, respectively) exhibited significantly improved fluorescence responses to depolarizing voltages compared with their predecessors in patch-clamp recordings from transfected cells [the ratio of fluorescence change to baseline fluorescence ($\Delta F/F$) values for 120-mV steps were (mean ± SEM) −31.3 ± 0.7% for Ace-mNeon2 ($n$ = 13 cells) versus −13.9 ± 0.6% for Ace-mNeon ($n$ = 11 cells), $P$ < 0.0001, Mann-Whitney test; and −22.9 ± 0.7% for VARNAM2 ($n$ = 13 cells) versus −14.1 ± 0.5% for VARNAM ($n$ = 8 cells), $P$ < 0.0001, Mann-Whitney test] (Fig. 1, C and D; figs. S3 to S5; and table S1).

We next screened a library of Ace-mNeon2 D92X positional mutants, owing to the highly conserved role of the N81/D92 (D, Asp) pair in opsin proton-pumping and photosensing (*33*, *34*). We uncovered several variants with response polarity reversals that exhibited fluorescence increases during depolarization (fig. S6). Although the best-performing positive variant Ace-mNeon2 D92N exhibited slower kinetics, reciprocal S81X saturation mutagenesis revealed kinetics rescue mutants (figs. S6 and S7). Among them, the S81D mutant also provided the largest voltage sensitivity. The 92N/81D reversed polarity phenotype is transposable across other Ace-based indicators, including VARNAM and Voltron (*13*, *18*).

For further engineering, we targeted residues lining Ace's photosensing helix C, amino acids involved in stabilizing its voltage-sensitive intermediate state, and those near the chromophore (Fig. 1A and fig. S1) (*34*–*36*). Voltage screening of mutagenic libraries uncovered positive variants with enhanced sensitivities (fig. S8). Ace-mNeon2 R78K S81D D92N W178F and VARNAM2 R78E S81D D92N, henceforth pAce (positive Ace) and pAceR (positive Ace in

[1]The John B. Pierce Laboratory, New Haven, CT 06519, USA. [2]Department of Cellular and Molecular Physiology, Yale University, New Haven, CT 06520, USA. [3]James H. Clark Center, Stanford University, Stanford, CA 94305, USA. [4]CNC Program, Stanford University, Stanford, CA 94305, USA. [5]Howard Hughes Medical Institute, Stanford University, Stanford, CA 94305, USA. [6]Department of Neuroscience, Yale University, New Haven, CT 06520, USA. [7]Kavli Institute of Neuroscience, Yale University, New Haven, CT 06520, USA. [8]Wu Tsai Institute, Yale University, New Haven, CT 06520, USA.
***Corresponding author. Email: mkannan@umn.edu (M.K.); gvasan@umn.edu (G.V.); mschnitz@stanford.edu (M.J.S.); vincent.pieribone@yale.edu (V.A.P.)**
†These authors contributed equally to this work.
‡Present address: Department of Neuroscience, University of Minnesota, Minneapolis, MN 55455, USA.

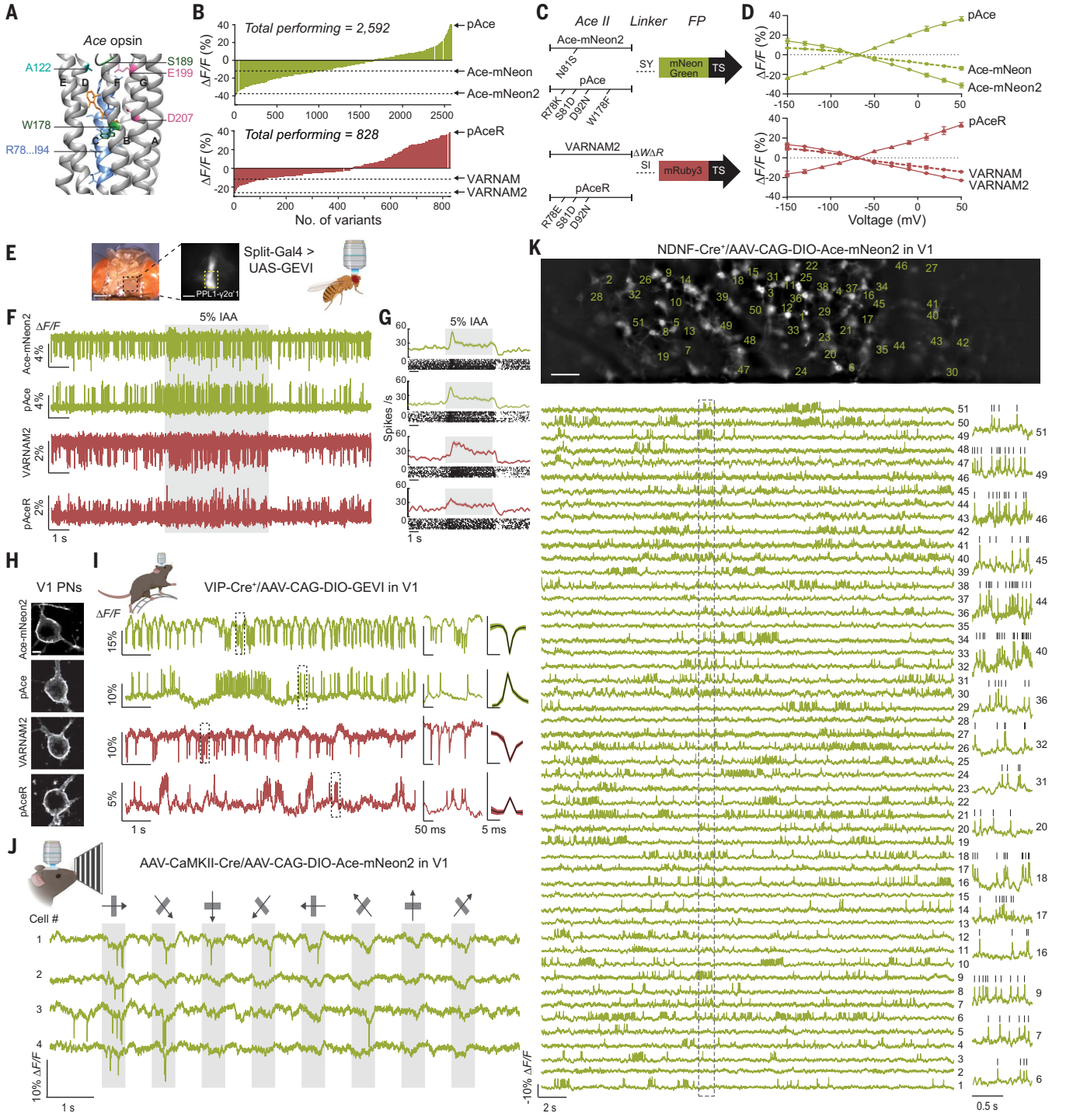


**Fig. 1. Design and characterization of Ace-mNeon2, VARNAM2 and reverse polarity variants pAce and pAceR.** (**A**) Crystal structure of Ace [Protein Data Bank (PDB) ID 3AM6], showing residues targeted for site-directed saturation mutagenesis on Ace-mNeon and VARNAM. The seven transmembrane helices are labeled A to G. Amino acids R78 through I94 on helix C and specified loci on other helices were targeted. A, Ala; W, Trp; R, Arg; I, Ile; S, Ser; E, Glu; D, Asp. (**B**) Distribution of fluorescence responses to field stimulation acquired from spiking HEK cells expressing Ace-mNeon (top) and VARNAM (bottom) variants obtained on the high-throughput platform. (**C**) Schematic representations of Ace-mNeon2, pAce, VARNAM2, and pAceR constructs, depicting the point mutations in Ace and the Ace-FP linker. SI is Ser, Ile; SY is Ser, Tyr; and TS is Thr, Ser. (**D**) *ΔF-ΔV* curves obtained using whole-cell recordings and concurrent fluorescence imaging of HEK cells transfected with Ace-mNeon, Ace-mNeon2, and pAce (top) and VARNAM, VARNAM2, and pAceR (bottom). Values represent mean ± SEM. (**E**) In vivo voltage imaging (left) through a transparent surgical window implanted on a fly head (graphic on right). Each of the indicators was selectively expressed in a PPL1-γ2α′1 dopaminergic neuron using a split-GAL4 system (center). The yellow dashed box indicates the axonal region of PPL1-γ2α′1. Scale bars, 200 μm (left) and 20 μm (right). (**F**) Representative recordings from PPL1-γ2α′1 using the four GEVIs, showing odor-evoked spiking elicited by 5-s delivery (gray shading) of 5% isoamyl acetate (IAA). (**G**) Spiking rates (mean ± SEM) during odor delivery and raster plots of individual trials in (F) (*n* = 10 trials, two trials

per fly). (**H**) Confocal images from coronal cortical slices of V1 PNs expressing the indicated sensors. Scale bar, 5 μm. (**I**) Example fluorescence traces showing spontaneous spiking obtained from awake, head-restrained mice selectively expressing the indicators in V1 VIP$^+$ interneurons (left); the boxed areas on the traces shown at an expanded time scale (center); and optical spike waveforms (mean ± SEM) (right) [$n$ = 5 neurons per condition ranked in order of decreasing signal-to-noise ratios, three mice each (Ace-mNeon2 and pAce) and two mice each (VARNAM2 and pAceR)]. (**J**) Example visual responses from layer 2/3 PNs to drifting gratings presented at eight different orientations, acquired using Ace-mNeon2 in an awake mouse. Arrows indicate stimulus orientation. Gray shading denotes stimulus periods. (**K**) Representative epifluorescence image of a single field of view from a NDNF-*Cre*$^+$ mouse expressing *Cre*-dependent soma-targeted Ace-mNeon2 in V1 (scale bar, 50 μm) (top) and $\Delta F/F$ traces showing spontaneous activity from the numbered cells (bottom). Fluorescence traces are inverted for visualization. The region enclosed by the dashed box is shown at an expanded time scale on the right for select cells. Gray ticks denote identified spikes.

Red), exhibited $\Delta F/F$ values of 36.6 ± 0.7% (mean ± SEM) and 33.4 ± 1.1% ($n$ = 11 cells each), respectively, per 120 mV in cultured HEK cells (Fig. 1, B to D; and figs. S5, S9, and S10) (E, Glu; F, Phe; K, Lys). Because these positive variants have the same signaling dynamic range as Ace-mNeon2 and VARNAM2 but in the opposite direction, they have slightly lower resting fluorescence intensities than the latter and reduced resting-state photobleaching, similar to other positive GEVIs (fig. S11) (*14*, *37*).

All indicators except pAceR showed submillisecond kinetics at room temperature (fig. S5 and table S1). Overall, Ace-mNeon2, VARNAM2, and pAce exhibited the largest effective $\Delta F/F$ (%) for single action potentials (APs) compared to prior negative- and positive-polarity GEVIs in 1-ms impulse response computations (fig. S12 and table S1).

### Sensor characterization in awake flies and mice

For voltage imaging in live animals for all studies described in this paper, we used high-speed (400 or 600 Hz in mice, 1 kHz in fruit flies), widefield one-photon epifluorescence microscopy. We first expressed each of our four GEVIs in the PPL1-γ2α′1 dopaminergic neuron in flies, in which they reported spontaneous and odor-evoked spiking with comparable baseline- and evoked spike rates (Fig. 1, E to G). Compared with their red counterparts, the green GEVIs exhibited greater response amplitudes and values of $d'$, a signal detection theory metric that characterizes how the ratio of fluorescence signals to background fluctuations sets the spike detection fidelity (*38*) [$\Delta F/F$, $d'$ (mean ± SEM): 3.1 ± 0.2%, 14.5 ± 1.4 (Ace-mNeon2); 4.0 ± 0.1%, 13.4 ± 0.8 (pAce); 1.1 ± 0.1%, 7.4 ± 0.4 (VARNAM2); 0.9 ± 0.03%, 6.5 ± 0.3 (pAceR)]. We also compared the performance of all four GEVIs in the PPL1-α′2α2 neuron, where they had greater $d'$ values than their parent indicators Ace-mNeon and VARNAM [~10.8 (Ace-mNeon2), ~8.7 (pAce), ~7.0 (VARNAM2), and ~6.7 (pAceR) versus reported values of ~6.9 (Ace-mNeon) and ~6.6 (VARNAM)] (fig. S13) (*18*). The higher $\Delta F/F$ values and superior photostability of pAce enabled extended duration (30 min) continuous recordings with stable $d'$ values throughout imaging sessions with illumination powers of ~5 mW mm$^{-2}$ (fig. S14).

For studies in live mice, our epifluorescence imaging methodology was designed to allow cellular resolution recordings in cortical brain tissue and to reduce both tissue autofluorescence and background fluorescence from scattered or out-of-focus indicator emissions. Specifically, we (i) were able to use modest illumination intensities (typically, 25 mW mm$^{-2}$), owing to the high brightness of our indicators; (ii) achieved relatively sparse fluorescence labeling (<370 labeled cells per mm$^2$) by targeting specific cell classes through virally mediated projection targeting or using cell type–specific *Cre*- or *Flp*-driver mouse lines (*39*–*42*); and (iii) generated soma-targeted versions of Ace-mNeon2, VARNAM2, pAce, and pAceR, which mainly trafficked to cell body membranes (Fig. 1H) (*43*). With this labeling and trafficking approach, <4.2% (and usually much less) of the area of each imaging plane was occupied by labeled cell bodies. Further, for data analyses, we used automated algorithms designed to extract neuronal activity traces with minimal contamination from physiologic artifacts or background activity (*44*–*46*) (fig. S15 and Materials and methods).

We expressed each of our four GEVIs in vasoactive intestinal peptide–expressing (VIP$^+$) interneurons in primary visual cortex (V1), in which they successfully reported single action potentials (Fig. 1, H and I). The $\Delta F/F$ values per spike (mean ± SEM) were −16.5 ± 1.9% for Ace-mNeon2 ($n$ = 127 spikes), 10.7 ± 1.4% for pAce ($n$ = 87 spikes), −7.3 ± 1.2% for VARNAM2 ($n$ = 49 spikes), and 3.2 ± 0.5% for pAceR ($n$ = 48 spikes).

To record stimulus-evoked activity, we used axonal projection targeting to express our best-performing GEVI, Ace-mNeon2, in a sparse subset of V1 layer 2/3 pyramidal neurons (PNs) ~100 to 200 μm beneath the pia (Fig. 2E). Specifically, we targeted PNs projecting to the anteromedial visual cortical area (AM) (*39*, *42*) by injecting an adeno-associated virus (AAV) expressing *Cre*-dependent Ace-mNeon2 into area V1 of wild-type mice along with a retrograde AAV expressing *Cre* under the CaMKII promoter into the AM. Voltage imaging of these V1→AM projecting neurons during presentations of drifting grating visual stimuli revealed the cells' orientation-selective visual responses (Fig. 1J).

To showcase imaging of neural ensemble dynamics, we used *Cre*-driver mice to target Ace-mNeon2 to neuron-derived neurotrophic factor–expressing (NDNF$^+$) interneurons, ~50 to 70 μm below the pia (*41*, *47*, *48*) (Fig. 2B), and recorded spiking in up to 51 cells at once (Fig. 1K) for 4 to 5 min continuously (fig. S16). Similarly, using other *Cre*- or *Flp*-driver lines, we respectively targeted Ace-mNeon2 or pAce to layer 2/3 somatostatin-expressing (SST$^+$) interneurons [~200 to 350 μm deep (*40*)] or VIP$^+$ interneurons [~50 to 300 μm below the pia (*49*)] to capture voltage signals from multiple cells of each neuron type (Fig. 2, C and D; and fig. S17). Across these different cortical subtypes, $d'$ values ranged from 9.9 to 17.5, implying spike detection error rates ranging from 0.04 spike min$^{-1}$ to infinitesimal values (fig. S18) (*38*). This high level of spike detection fidelity allowed us to extract spike trains and spike timing estimates that were invariant to the use of different cell-extraction algorithms (fig. S15, A, B, D, and G).

### Voltage imaging of visual cortical ensembles during behavioral state transitions

In neocortex, interneuron activity is strongly influenced by an animal's internal state and, in turn, modulates excitatory cells (*1*–*5*). However, the extent to which different interneuron types respond to state transitions and how distinct brain states affect the millisecond-scale interactions between subtypes remain unknown.

To address these questions, we selectively targeted Ace-mNeon2 to NDNF$^+$, VIP$^+$, or SST$^+$ interneurons in area V1, or to V1→AM projecting neurons, by using the same mouse lines and viruses as described earlier in the text (Fig. 2A) (*40*, *41*). Voltage imaging in V1 of awake, head-restrained mice revealed spontaneous spiking rates (mean ± SEM) of 4.72 ± 0.01 Hz for NDNF$^+$ neurons ($n$ = 192 cells, seven mice), 6.52 ± 0.23 Hz for VIP$^+$ neurons ($n$ = 49 cells, five mice), 4.71 ± 0.21 Hz for SST$^+$ neurons ($n$ = 43 cells, five mice), and 0.93 ± 0.34 Hz for PNs ($n$ = 53 cells, five mice). These values are consistent with estimated spike rates of V1 layer 2/3 PNs and SST$^+$ cells obtained using electrophysiological recordings in awake mice (*4*, *50*). Likewise, the higher spontaneous firing rates of VIP$^+$ versus SST$^+$ interneurons have been observed across distinct cortical areas (*51*, *52*).

To induce a change in brain state by increasing arousal, we delivered a brief air puff to the mouse's back while monitoring its pupil

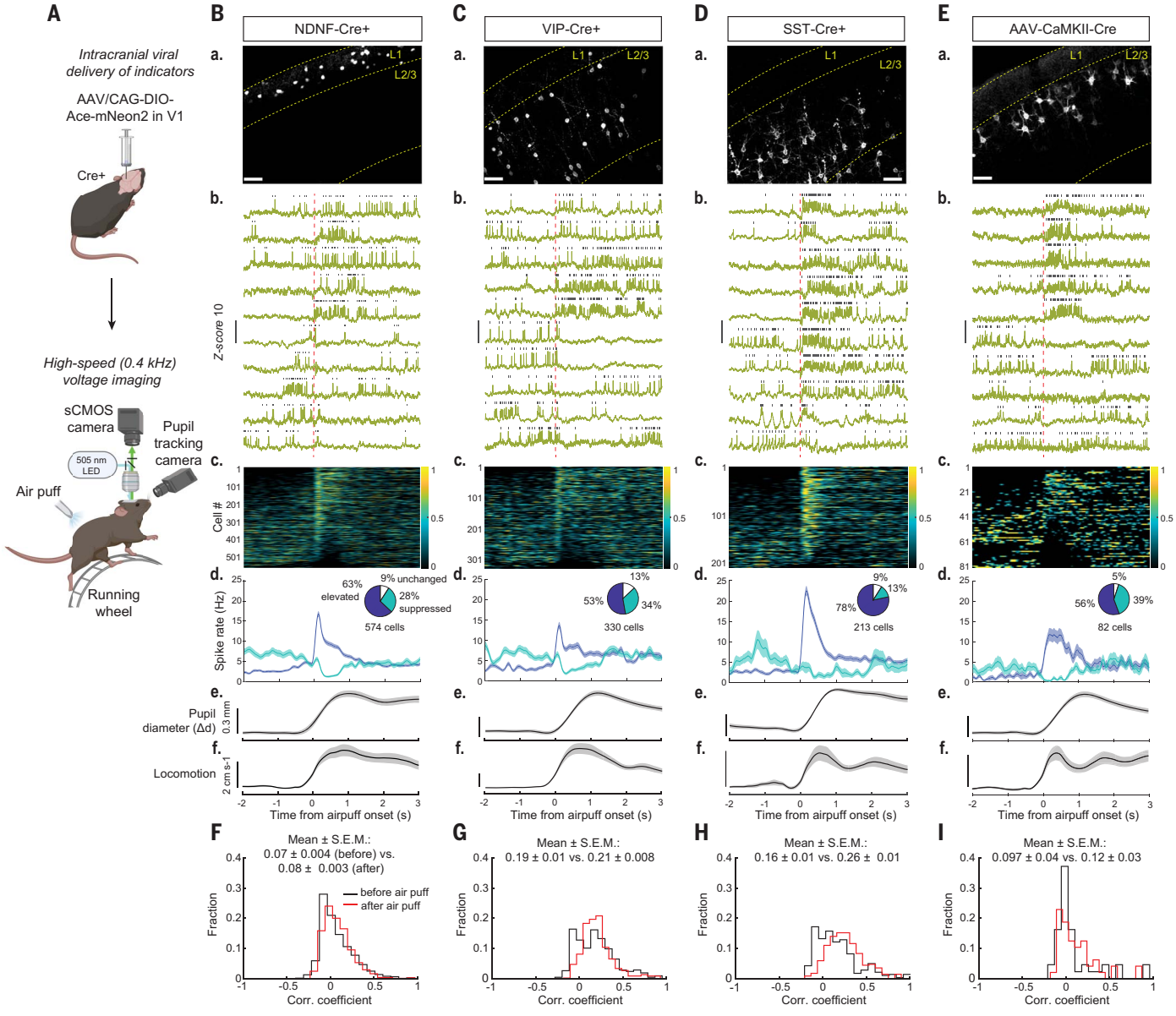


**Fig. 2. Ace-mNeon2 voltage imaging unveils state-dependent modulation of spontaneous firing in excitatory and inhibitory cell types in V1.** (**A**) Schematic of AAV injection and experimental setup. LED, light-emitting diode; sCMOS, scientific complementary metal oxide semiconductor. (**B**) Ace-mNeon2 voltage imaging of NDNF$^+$ neurons during air puff delivery. (a) Confocal images of soma-targeted Ace-mNeon2 expression in NDNF$^+$ interneurons. Scale bar, 50 μm. (b) Representative fluorescence-time traces from individual cells (inverted for visualization purposes). The vertical dashed line in red indicates air-puff onset. Gray ticks denote identified spikes. (c) *Z*-scored firing rate for all NDNF$^+$ interneurons ($n$ = 574 cells, six mice). Cells are arranged in order of decreasing spike modulation indices (Materials and methods). (d) Firing rate (mean ± SEM) aligned to air-puff onset for activated (dark blue) and suppressed (cyan) fractions. Pie chart insets indicate the percentage of cells with increased (dark blue), suppressed (cyan), or unchanged (white) spike rates after air puff. (e) Pupil diameter (mean ± SEM). (f) Locomotor speed (mean ± SEM). (**C**) Same as (B) for VIP$^+$ interneurons ($n$ = 330 cells, five mice). (**D**) Same as (B) for SST$^+$ interneurons ($n$ = 213 cells, six mice). (**E**) Same as (B) for PNs ($n$ = 82 cells, four mice). (**F**) Distribution of pairwise correlation coefficients of mean firing rates across a sliding 20-ms window, as determined for 3-s intervals, before (black) and after (red) air puff for NDNF$^+$ interneurons (2300 cell pairs in the same fields of view, six mice; $P$ = 0.0021; Wilcoxon matched-pairs signed rank test for before versus after air puff). The mean ± SEM correlation coefficient values are shown above the distribution plots. (**G**) Same as (F) for VIP$^+$ interneurons ($n$ = 442 pairs, five mice; $P$ = 0.0011). (**H**) Same as (F) for SST$^+$ interneurons ($n$ = 334 pairs, six mice; $P$ < 0.0001). (**I**) Same as (F) for PNs ($n$ = 51 pairs, four mice; $P$ = 0.03).

diameter, which is a commonly used, simple metric of arousal (Fig. 2A) (*53*, *54*). The evoked arousal was often accompanied by the onset of locomotion and robust modulations of spiking across all neuron classes studied (Fig. 2, B to E). However, the distinct cell classes differed regarding both the fractions of cells that increased or decreased their spiking and the magnitudes of spike rate modulation (Fig. 2, B to E).

We imaged the spiking dynamics of ~1200 neurons across the different cell types. Upon arousal, SST$^+$ interneurons exhibited the most substantial state-dependent modulation, with 78% of SST$^+$ cells increasing their spontaneous spiking rates and only 13% decreasing their spiking rates (Fig. 2D). SST$^+$ cells also underwent the greatest increases in spike rates among the cell types imaged, from 2.5 ± 0.4 Hz (mean ±

SEM) under baseline conditions to 22.5 ± 1.2 Hz after air puff (Fig. 2D). Sixty-three percent of NDNF$^+$ interneurons also increased their spiking, from 2.6 ± 0.3 to 16.8 ± 0.7 Hz, whereas 28% decreased their spiking after air puff (Fig. 2B). VIP$^+$ neurons and PNs exhibited comparable state-dependent responses, with half of each population showing increased spiking (53 and 56%, respectively) and a third showing suppressed spiking (34 and 39%, respectively) after air puff. These latter two classes also had similar spike rate increases during arousal (from 3.8 ± 0.5 to 13.7 ± 0.8 Hz for VIP$^+$ cells and 0.9 ± 0.3 to 11.8 ± 1.6 Hz for PNs) (Fig. 2, C and E). That each neuron type that we studied exhibited a subset of cells that decreased their spiking argues against the possibility that the net spiking increases were motion-related artifacts stemming from the locomotion that often occurred after the air puff. Further supporting this point, during air-puff trials in which there was no locomotor increase, we still observed comparable modulations in neural activity (fig. S19). Among the cell types imaged, the air puff–evoked rise in spiking among SST$^+$ cells returned the fastest toward baseline levels, whereas VIP$^+$ and NDNF$^+$ interneurons, which receive inhibitory inputs from SST$^+$ cells (*47*, *55*), returned more gradually to baseline spiking levels (Fig. 2, B to D).

To characterize the degree of spiking synchronization between the cells of each type, we computed pairwise correlation coefficients for the time-dependent spike rates of each cell pair and compared the distributions of these coefficients as determined before versus after air puff. Both SST$^+$ and VIP$^+$ cells exhibited positive intrapopulation coupling of spontaneous activity (*56*), which rose slightly during arousal, especially among SST$^+$ cells. By comparison, NDNF$^+$ interneurons and PNs showed weaker intrapopulation correlations (*57*), which were unaltered by air puff (Fig. 2, F to I).

### Dual polarity multiplexed voltage imaging

Although arousal increases the net spontaneous activity of multiple cell subtypes (Fig. 2), how it alters the fine-scale dynamic relationships between two or more subtypes remains unknown. Thus, we turned to simultaneous multipopulation voltage imaging using our improved GEVIs.

Multipopulation recordings using fluorescent $Ca^{2+}$ or voltage sensors were previously done by targeting spectrally orthogonal sensors to distinct cell types (*18*, *58*–*61*). We reasoned that a pair of GEVIs operating in the same spectral channel but with opposite response polarities should be mutually compatible, allowing studies of two cell types per color channel. The cells of each type can be distinguished by the directionality of their optical spike waveforms (fig. S20).

We performed dual-polarity multiplexed voltage imaging (DUPLEX) in awake mice, where we targeted Ace-mNeon2 and pAce either to two distinct inhibitory or to one excitatory and one inhibitory cell type by using *Cre*- and *Flp*-dependent expression strategies (Fig. 3A and Materials and methods). We virally expressed *Cre*-dependent Ace-mNeon2 and *Flp*-dependent pAce in area V1 of NDNF-*Cre*$^+$/VIP-*Flp*$^+$ or SST-*Cre*$^+$/VIP-*Flp*$^+$ double-transgenic mice (Fig. 3, B to G). Alternatively, we injected recombinase-dependent Ace-mNeon2 and pAce viruses along with AAV-CaMKII-*Cre* into VIP-*Flp*$^+$ mice (fig. S21). High-speed epifluorescence imaging in a single color channel revealed the joint dynamics of NDNF$^+$ and VIP$^+$ cells, SST$^+$ and VIP$^+$ cells, or PNs and VIP$^+$ cells, respectively, in these mice while they were awake but head restrained (Fig. 3, B to G; and fig. S21).

To estimate the degree of functional connectivity within and across cell types, we computed pairwise correlation coefficients for the time ($t$)–varying activity traces, $\Delta F/F(t)$, as well as for the spike rates of cell pairs in the same fields of view. NDNF$^+$ and VIP$^+$ interneurons had positive intrapopulation correlations but NDNF$^+$- VIP$^+$ pairs had virtually uncorrelated dynamics (Fig. 3, D, H, and I). The mean ± SEM correlation coefficients were 0.19 ± 0.02 ($\Delta F/F$) and 0.15 ± 0.02 (spike rates) for NDNF$^+$-NDNF$^+$ pairs, 0.31 ± 0.04 ($\Delta F/F$) and 0.29 ± 0.09 (spike rates) for VIP$^+$-VIP$^+$ pairs, and −0.09 ± 0.04 ($\Delta F/F$) and 0.02 ± 0.02 (spike rates) for NDNF$^+$-VIP$^+$ pairs (Fig. 3I), in accord with reports that the two subtypes may receive distinct inputs or not strongly target each other (*47*, *48*).

By comparison, DUPLEX imaging of SST$^+$ and VIP$^+$ cells revealed slightly negatively correlated intertype dynamics, whereas the intratype dynamics were positively correlated [mean ± SEM correlation coefficients were 0.37 ± 0.04 ($\Delta F/F$) and 0.11 ± 0.03 (spike rates) for SST$^+$-SST$^+$ pairs, 0.51 ± 0.05 ($\Delta F/F$) and 0.30 ± 0.07 (spike rates) for VIP$^+$-VIP$^+$ pairs, and −0.22 ± 0.04 ($\Delta F/F$) and −0.04 ± 0.01 (spike rates) for SST$^+$-VIP$^+$ pairs] (Fig. 3, G, J, and K). DUPLEX imaging of PNs and VIP$^+$ cells revealed very low correlations between the two neuron types [−0.009 ± 0.03 ($\Delta F/F$) and 0.06 ± 0.02 (spike rates)], whereas the intrapopulation correlation coefficients were higher [0.23 ± 0.10 ($\Delta F/F$) and 0.15 ± 0.08 (spike rates) for PN pairs; 0.32 ± 0.07 ($\Delta F/F$) and 0.16 ± 0.05 (spike rates) for VIP$^+$-VIP$^+$ pairs] (Fig. 3, L and M; and fig. S21).

To examine how spiking by one interneuron subtype relates to membrane potential dynamics of cells in the same or another interneuron subtype, we computed cross-correlation functions between one cell's spike rate and the subthreshold part of another cell's time-varying activity trace, $\Delta F/F(t)$, averaged over all pairs of cells of the two subtypes in the same field of view (fig. S22). The results verified that SST$^+$ and VIP$^+$ cells had positive intrapopulation correlations, whereas SST$^+$-VIP$^+$ pairs had negatively correlated dynamics, and that the dynamics of NDNF$^+$ cells were only weakly correlated with those of other NDNF$^+$ cells and VIP$^+$ cells. These results are consistent with paired recordings in live-brain slices that have revealed a bidirectional inhibition between SST$^+$ and VIP$^+$ neurons and nonoverlapping synaptic inputs to the two subtypes (*55*, *62*).

### DUPLEX imaging in hippocampal area CA1

Past studies using GEVIs have assessed relationships between specific neuron classes and the local field potential (LFP) in hippocampal area CA1 (*23*, *63*). Using DUPLEX imaging, we tracked the concurrent dynamics of two CA1 neuron classes by expressing our two red GEVIs in distinct cell types (fig. S23) or by using our two green GEVIs in tandem while also recording LFPs (Fig. 4A and fig. S24). In a running mouse expressing Ace-mNeon2 in entorhinal cortex (EC)–projecting excitatory neurons in the *stratum pyramidale* (~150 to 200 μm below a glass window) and pAce in SST$^+$ interneurons in the *stratum oriens* (~25 to 150 μm below a glass window), we tracked 10 excitatory and 18 SST$^+$ cells in the same field of view and distinguished the two cell types by the opposing polarities of their optical spike waveforms (Fig. 4, B to D). Spike detection fidelity indices ($d'$) in CA1 neurons ranged from 10.6 to 17.6, implying spike detection error rates of 0.007 spike min$^{-1}$ or less (fig. S18) (*38*).

SST$^+$ interneurons had greater baseline spike rates and burstiness than the EC-projecting neurons [19.8 ± 1.8 versus 14.7 ± 0.5 Hz (mean ± SEM), $P < 0.01$] (Fig. 4E). We assessed the extent to which spiking by the excitatory and inhibitory neurons was phase-locked to membrane potential oscillations in these specific cell types or to CA1 LFP signals. Across a total of 157 neurons, spiking from both cell types was locked with greater precision to intrapopulation subthreshold oscillations than to the LFP; notably, SST$^+$ cells and EC-projecting PNs spiked at distinct phases of their intrinsic theta (4 to 9 Hz) membrane potential dynamics [13.8° ± 2.6° and −1.3 ± 4.8°, respectively (mean ± SEM, $P < 0.01$)] (Fig. 4, F to H). Spiking in EC-projecting cells but not SST$^+$ cells also consistently phase-locked to the LFP ($P < 0.001$ and $P = 0.82$, respectively) (Fig. 4, G and H).

We next assessed the relationships between the LFP and the cell type–specific subthreshold dynamics, as well as those between the subthreshold dynamics of the two subtypes. We found strong subthreshold coherence between both cell types and the LFP in the theta frequency band ($P < 0.0001$ and $P < 0.0001$, respectively) (Fig. 4, I to L; and fig. S24, A to D). We also found strong intra- and

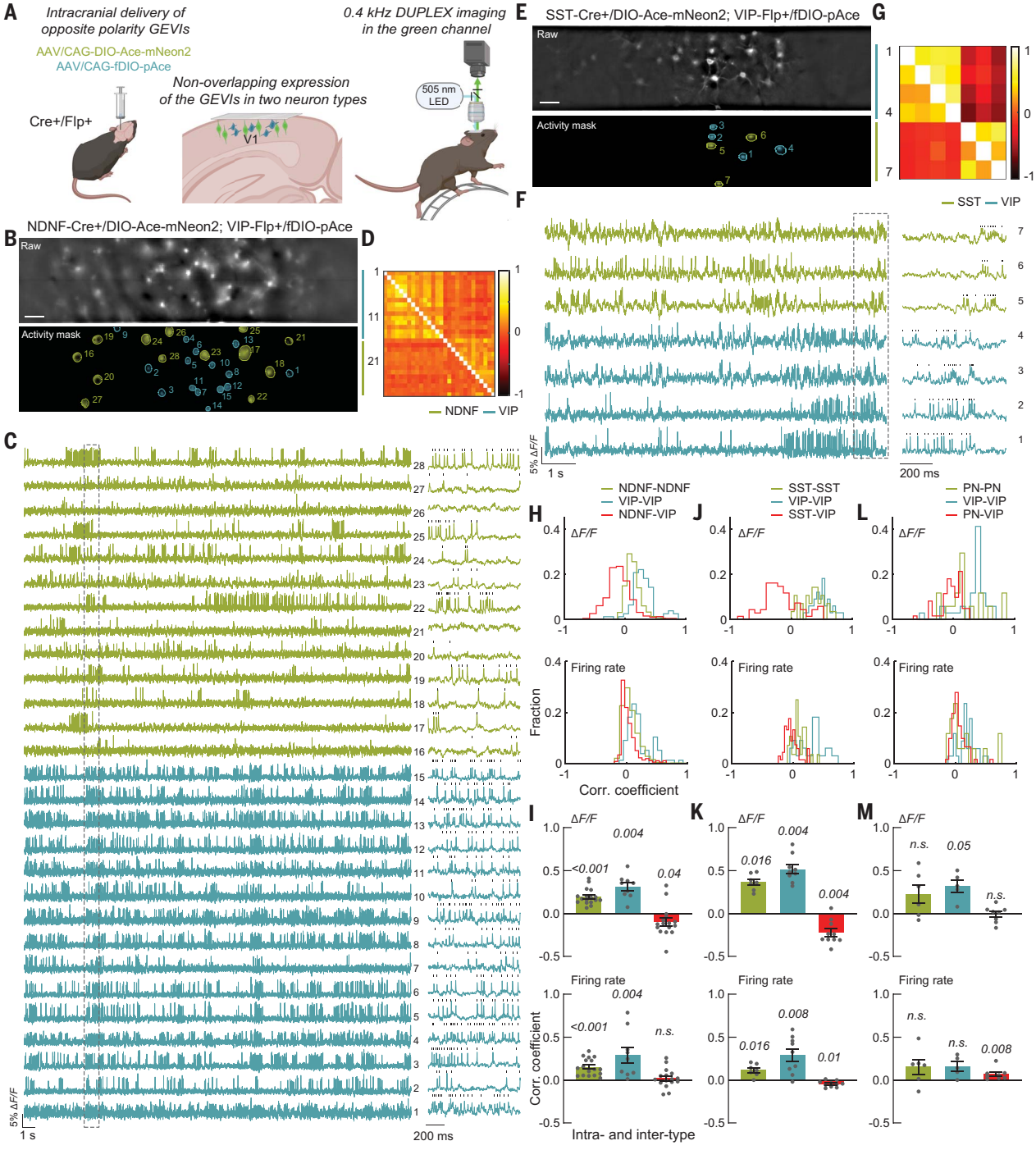


**Fig. 3. DUPLEX captures the concerted activation dynamics between cell types in V1.** (**A**) Schematic of AAV injections and experimental setup. (**B** to **G**) Example DUPLEX recordings from two targeted cortical cell types. (B) and (E) show raw epifluorescence (top) and activity-mask (bottom) images of single fields of view from a (B) NDNF-*Cre*$^+$/VIP-*Flp*$^+$ mouse expressing Ace-mNeon2 in NDNF$^+$ interneurons (green) and pAce in VIP$^+$ cells (blue) and (E) SST-*Cre*$^+$/VIP-*Flp*$^+$ mouse expressing Ace-mNeon2 in SST$^+$ interneurons (green) and pAce in VIP$^+$ interneurons (blue). Active cells are numbered. Scale bar, 50 μm. (C) and (F) show Δ*F*/*F* traces from the cells numbered in (B) and (E), respectively. Ace-mNeon2 traces are inverted for visualization purposes. The regions enclosed by the dashed boxes in (C) and (F) are shown at an expanded time scale to the right. Gray ticks indicate identified spikes. (D) and (G) show intra- and interpopulation correlation coefficient matrices of pairwise, zero time-lag correlation coefficients of the Δ*F*/*F* traces (upper triangle) and spiking rates (lower triangle), determined using a 20-ms sliding window for the cells in (C) and (F), respectively. (**H**) Distribution of pairwise correlation coefficients for Δ*F*/*F* traces (top) and spiking rates (bottom) across all mice for NDNF/VIP recordings ($n$ = 1795 NDNF-NDNF pairs, 77 VIP-VIP pairs, and 373 NDNF-VIP pairs; 208 NDNF-neurons and 54 VIP-neurons, five mice). (**I**) Mean ± SEM pairwise correlation coefficients for Δ*F*/*F* traces (top) and spiking rates (bottom) for the NDNF/VIP dataset in (H) ($n$ = 17 fields of view). $P$ values are italicized (one-sample Wilcoxon test against zero). n.s., not significant. (**J** and **K**) Same as (H) and (I) for SST/VIP recordings ($n$ = 28 SST-SST pairs, 33 VIP-VIP pairs, and 67 SST-VIP pairs; 25 SST$^+$ neurons and 29 VIP$^+$ neurons, 10 fields of view, three mice). (**L** and **M**) Same as (H) and (I) for PN/VIP recordings ($n$ = 17 PN-PN pairs, 34 VIP-VIP pairs, and 61 PN-VIP pairs; 20 PNs and 22 VIP$^+$ neurons, eight fields of view, three mice).

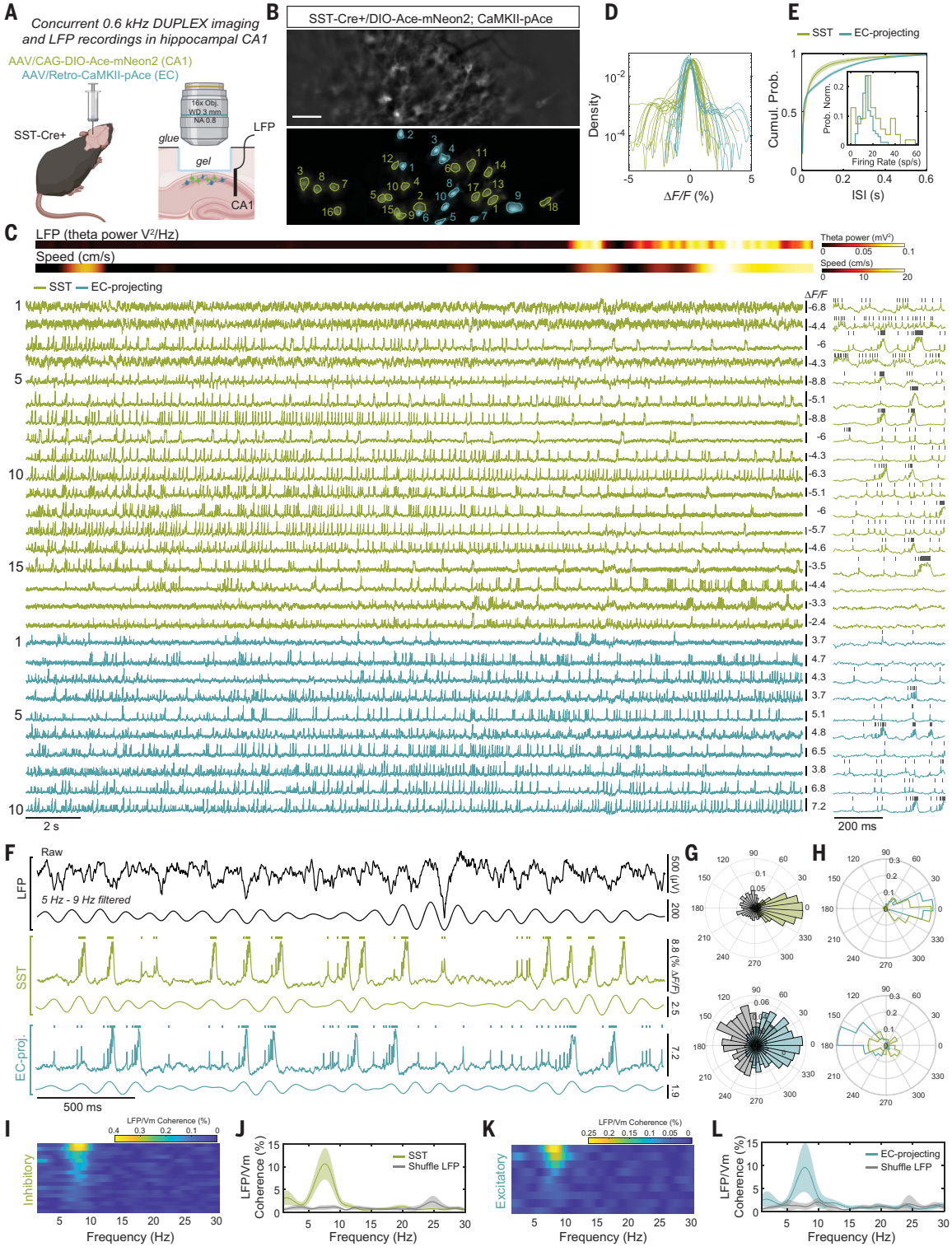


**Fig. 4. DUPLEX uncovers cell class–specific contributions to the LFP in hippocampal CA1.** (**A**) Schematic of AAV injections and experimental setup. (**B**) Representative raw epifluorescence image (top) and spatial footprint of negative-polarity signals (green) and positive-polarity signals (blue) of 18 and 10 identified neurons, respectively (bottom). Scale bar, 50 μm. (**C**) Δ*F*/*F* traces (bottom) for all the neurons in (B) along with wheel speed and LFP theta (top). Ace-mNeon2 traces are inverted for visualization purposes. The first 500 ms are shown at the expanded time scale to the right. Gray ticks denote identified spikes. (**D**) Fluorescence trace amplitude distributions for all neurons across all fields of view. Note the opposite polarities within similar dynamic ranges for Ace-mNeon2 and pAce. (**E**) Cumulative distributions of interspike intervals (ISIs) and firing rates (inset; sp/s, spikes per second) for all recorded neurons ($n$ = 55 SST$^+$ interneurons and 102 projection neurons, six fields of view, one mouse). The shaded area represents the 95% confidence interval (CI). (**F**) Phase relationships between spike and theta oscillations extracted from the LFP or cellular transmembrane voltage oscillations for projection neurons and SST$^+$ cells recorded simultaneously. Shown here are the raw LFP trace (top) and the theta-filtered (5 to 10 Hz) (center) and unfiltered (bottom) excitatory and inhibitory

traces. (**G**) Spike-theta phase relationship for the two neurons in (F). Color and gray represent the optically acquired theta transmembrane voltage ($V_m$) and theta LFP, respectively. Note that both neurons are phase-locked to their own $V_m$ and to the LFP but with approximately opposite phases. (**H**) Polar histogram of the probability density of the average spike-theta phase relationship for all 157 neurons, computed against their respective theta $V_m$ (top) or theta LFP (bottom). For each neuron, average spike timing relative to the theta cycle was computed using the circular mean. (**I** to **L**) LFP-subthreshold coherence of all neurons in (C), showing that a fraction of [(I) and (J)] $SST^+$ interneurons and [(K) and (L)] EC-projecting excitatory neurons are phase-locked to theta LFP. For (I) and (K), raster plots are sorted in decreasing order of theta-band coherence strength. For (J) and (L), LFP coherence is averaged across all neurons in (I) and (K). The shaded area represents the 95% CI.

interpopulation coherence in the beta frequency band (15 to 25 Hz) (fig. S24, E to H), in contrast to the lack of beta frequency band coherence with the LFP (fig. S24, A to D).

### DUPLEX imaging in live flies

To showcase the use of DUPLEX for multi–cell type recordings across species, we expressed pAce in the γ-aminobutyric acid–signaling (GABAergic) MBON-γ1pedc>α/β neuron and Ace-mNeon2 in the PPL1-α′2α2 dopaminergic neuron in fruit flies (fig. S25A). Both these cells receive excitatory olfactory inputs from mushroom body Kenyon cells, and MBON-γ1pedc>α/β also exerts feedback inhibition onto PPL1-α′2α2 axons (*64*). When we exposed the double-labeled flies to odorants, DUPLEX imaging of PPL1-α′2α2 axons and MBON-γ1pedc>α/β dendrites revealed that MBON-γ1pedc>α/β was strongly activated throughout exposure to an attractive odor [apple cider vinegar (ACV)] but was more transiently activated by a repulsive odor [benzaldehyde (BEN)]. By contrast, PPL1-α′2α2 was strongly inhibited by ACV but weakly excited by BEN, in accord with the known inhibitory connection from MBON-γ1pedc>α/β to PPL1-α′2α2 (fig. S25, B and C).

### Interpopulation correlations of spiking dynamics during state transitions

We next used DUPLEX to examine how state transitions affect the interactions between cortical subtypes. In green DUPLEX recordings from $NDNF^+$ and $VIP^+$ interneurons in layer 1 of V1 (~50 to 100 μm below the pia), spike rates were uncorrelated across the two populations under baseline conditions (Fig. 5, A to C), and air puff–induced arousal had no impact on this uncorrelated behavior [mean ± SEM correlation coefficients: 0.07 ± 0.02 before air puff versus 0.10 ± 0.03 after] (Fig. 5C). To quantify the effects of air puff on the spiking of individual cells, we also computed a spike modulation index from −1 to 1 (Material and methods). Spiking by $NDNF^+$ and $VIP^+$ cells was significantly positively modulated by air puff [mean ± SEM; median values: 0.27 ± 0.02; 0.32 ($P < 0.0001$, one-sample Wilcoxon signed rank test against zero) and 0.11 ± 0.03; 0.08 ($P = 0.006$), respectively] (Fig. 5D).

In DUPLEX recordings from $SST^+$ and $VIP^+$ interneurons (~200 to 250 μm below the pia), spiking by the two subtypes became significantly more anticorrelated after air puff (mean ± SEM correlation coefficients: −0.02 ± 0.01 before air puff versus −0.14 ± 0.03 after) (Fig. 5, E to G). The spike modulation indices also revealed that most $SST^+$ cells were positively modulated by the air puff [mean ± SEM; median values: 0.43 ± 0.05; 0.57 ($P < 0.0001$, one-sample Wilcoxon test)], whereas $VIP^+$ cells imaged concurrently at the same tissue depth and in the same fields of view more commonly had negative values of the spike modulation index [mean ± SEM; median values: −0.07 ± 0.05; −0.12 ($P = 0.14$)] (Fig. 5H).

DUPLEX studies in PNs and $VIP^+$ cells (~150 to 200 μm below the pia) revealed uncorrelated dynamics for these cell classes before and after air puff (mean ± SEM correlation coefficients were 0.04 ± 0.02 before versus 0.05 ± 0.02 after air puff) (Fig. 5, I to K). The spike modulation indices revealed a small positive modulation of both populations by the air puff [mean ± SEM; median values: 0.19 ± 0.09; 0.44 ($P = 0.06$, one-sample Wilcoxon test) and 0.08 ± 0.05; 0.07 ($P = 0.14$), respectively] (Fig. 5L).

### Dual-color voltage imaging of hippocampal projection neurons

Although DUPLEX can dissect activity patterns among nonoverlapping populations, such as discrete excitatory and interneuron subtypes, when the level of overlap between two neuronal subclasses is unknown, their activities can instead be distinguished by simultaneous dual-color voltage imaging. We used Ace-mNeon2 and VARNAM2 to examine the extent to which two subclasses of CA1 projection neurons, targeting distinct cortical regions, modulate their spiking during a rest-to-run behavioral transition. We expressed Ace-mNeon2 and VARNAM2 in anterior cingulate cortex (ACC)– and EC-projecting CA1 PNs, respectively, using retrograde AAV labeling. We then performed simultaneous dual-color voltage imaging in an injected mouse, which was head restrained on a running wheel, and used a brief air puff to elicit a rest-to-run behavioral transition (Fig. 5M).

We imaged a total of 101 ACC-projecting and 34 EC-projecting neurons from five fields of view in the same animal, with a single field of view containing as many as 30 and 13 cells of the two subclasses, respectively (Fig. 5, M and N; and fig. S26). Both Ace-mNeon2 and VARNAM2 captured a diversity of cell dynamics, including isolated spikes, spike bursts, and subthreshold oscillations.

We assessed whether the ACC- and EC-projecting cell ensembles had distinct supra- and subthreshold dynamics across the behavioral state transition (*6*–*9*). Whereas EC-projecting cells did not significantly change their spike rates after the onset of locomotion, ACC-projecting cells did [$\log_2$ fold change (mean ± SEM): 0.0 ± 0.2 for EC-projecting cells versus 0.9 ± 0.1 for ACC-projecting cells; $P = 0.59$ and $P < 0.0001$; rank sum test between real data and spike trains circularly permuted in time] (Fig. 5, O to Q; and fig. S26). We also observed greater coherence in subthreshold activity after the behavioral transition, but interestingly, each subclass synchronized at distinct frequencies (7.3 ± 0.3 and 4.2 ± 0.2 Hz, respectively, for ACC- and EC-projecting cell pairs; $P < 0.0001$; rank sum test computed for run epochs against levels estimated from neurons belonging to different fields of view) (Fig. 5, R to T).

### Simultaneous voltage imaging of three cell populations

Together, our indicators enable discriminations of distinct targeted subtypes or projection-specific cell subclasses based on the polarity of optical spike waveforms as well as spectral orthogonality. Thus, in principle, the four GEVIs are mutually compatible and allow recordings from up to four distinct neuron types at once. To demonstrate dual polarity and dual-color multiplexing, we performed proof-of-concept voltage imaging from three distinct cell populations simultaneously.

In an SST-*Cre*$^+$/VIP-*Flp*$^+$ double-transgenic mouse, we injected AAVs encoding both *Cre*-dependent Ace-mNeon2 and *Flp*-dependent pAce into V1, along with a retrograde AAV expressing CaMKII-VARNAM2 in area AM to label a subset of excitatory projection neurons (Fig. 6A). We then performed voltage imaging in V1 using dual-color, widefield epifluorescence microscopy to record from $SST^+$, $VIP^+$, and excitatory neurons concurrently (Fig. 6, B and C).

To image three neuron classes at once in the hippocampus, we retrogradely labeled EC- and lateral septum (LS)–projecting CA1 PNs and $SST^+$ interneurons, using viruses to express Ace-mNeon2, pAce, and pAceR, respectively, in a SST-*Cre*$^+$ mouse (Fig. 6D). With simultaneous dual-color imaging, we captured the concurrent spiking and subthreshold activity of as many as 57 cells in one field of view belonging to the three subpopulations (21 EC-projecting, 15 LS-projecting, and 21 $SST^+$ cells). These ensembles comprised nonoverlapping cell populations (Fig. 6E), and all three GEVIs reported spiking at high signal-to-noise ratios (Fig. 6F).

### Conclusion

Our suite of mutually compatible GEVIs allows simultaneous high-speed voltage imaging of

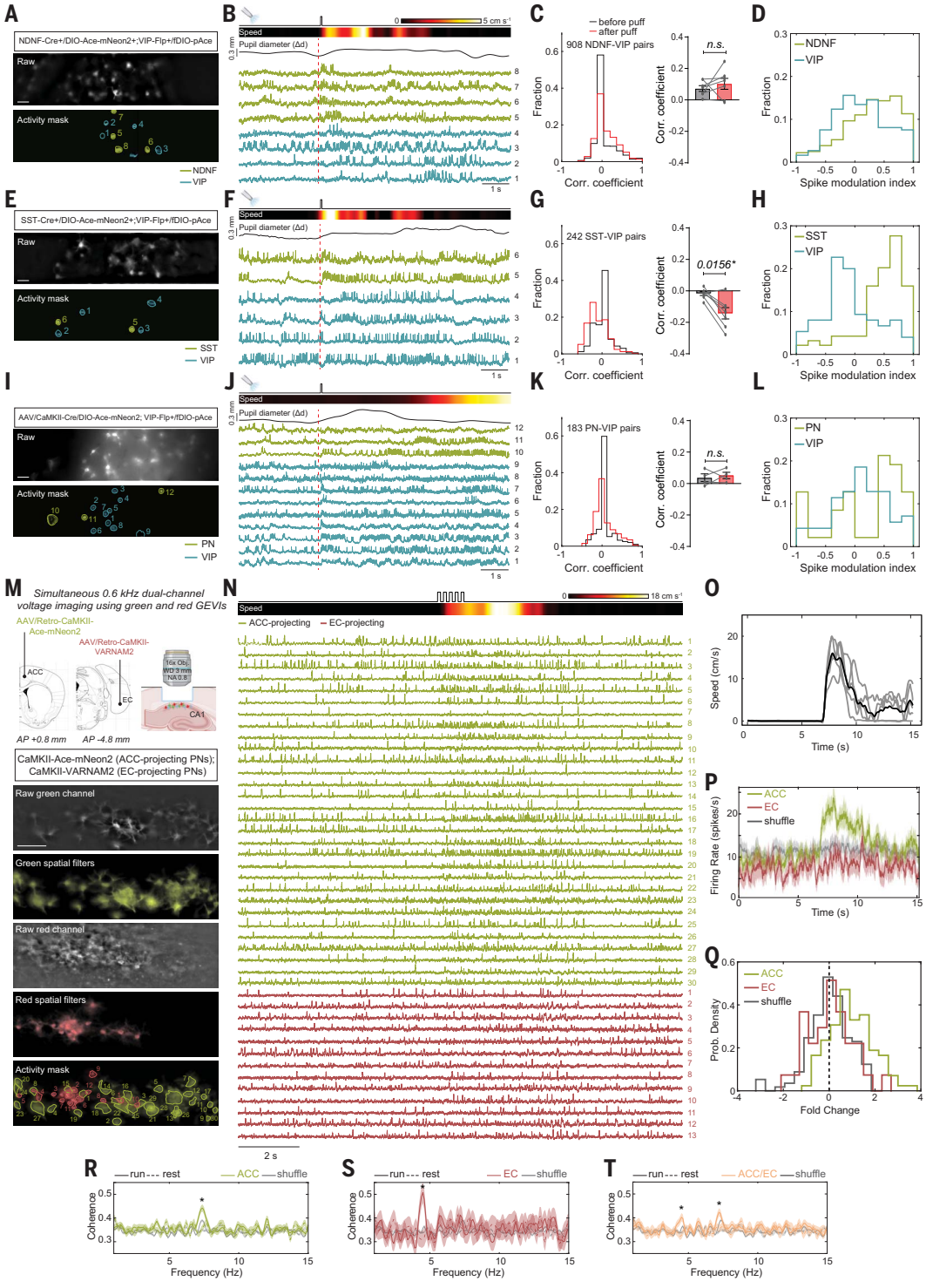


**Fig. 5. Dual population recordings in V1 and CA1 during state transitions.** DUPLEX recordings in V1 are shown in (A) to (L). (**A**) Representative raw epifluorescence (top) and activity-mask (bottom) images of a single field of view from a NDNF-*Cre*$^+$/VIP-*Flp*$^+$ mouse expressing Ace-mNeon2 in NDNF$^+$ interneurons (green) and pAce in VIP-cells (blue). Scale bar, 50 μm. (**B**) Δ*F*/*F* traces from the cells numbered in (A) aligned to air-puff onset (vertical dashed line). Ace-mNeon2 traces are inverted for visualization purposes. Also shown at the top are air-puff onset, locomotion speed, and pupil diameter. (**C**) Distribution of pairwise intertype correlation coefficients of spike rates (left) determined using a 20-ms sliding window for a 3-s interval before (black) or after (red) air puff ($n$ = 908 NDNF-VIP pairs from 393 NDNF$^+$ and 188 VIP$^+$ cells, seven mice) and mean ± SEM correlation coefficients by mouse (right) ($n$ = 7 mice; one-tailed Wilcoxon matched-pairs signed rank test). (**D**) Distribution of spike modulation indices for all NDNF$^+$ and VIP$^+$ neurons in (C). (**E** to **G**) Same as (A) to (C) for DUPLEX recordings in SST-*Cre*$^+$/VIP-*Flp*$^+$ mice ($n$ = 242 SST-VIP pairs from 103 SST$^+$ and 79 VIP$^+$ cells, six mice; *$P$ < 0.05, one-tailed Wilcoxon matched-pairs signed rank test). (**H**) Same as (D) for all SST$^+$ and VIP$^+$ neurons. (**I** to **K**) Same as (A) to (C) for DUPLEX recordings in AAV-CaMKII-*Cre*/VIP-*Flp*$^+$ mice ($n$ = 183 PN-VIP pairs from 75 PNs and 67 VIP$^+$ cells, four mice; one-tailed Wilcoxon matched-pairs signed-rank test). (**L**) Same as (D) for all PNs and VIP$^+$ neurons. Dual-color voltage recordings from hippocampal projection neurons are shown in (M) to (T). (**M**) Schematic of the experimental approach (top) and representative field of view of the red and green channels in grayscale, their respective overlay of spatial filters estimated by EXTRACT for each spiking neuron in each spectral channel, and the overlay of the spatial filter contours for all 30 and 13 identified projection specific neurons, respectively (bottom). Scale bar, 50 μm. (**N**) Δ*F*/*F* traces for all neurons in (M), aligned to the rest-run transition. Also shown at the top are the onset of five consecutive air puffs and wheel speed. (**O**) Average mouse speed for five trials (black). Individual trials are shown in gray. (**P**) Average firing rate (250-ms window) for each projection-specific class. Shuffle is computed by random circular permutations of each neuron's spike train. The shaded area represents the 95% CI. (**Q**) Fold-change in the cells' spiking rates, computed across 2-s intervals before and after air puff. Shuffle is computed using a random circular permutation of each neuron's spike train. (**R** to **T**) Average pairwise coherence of the subthreshold dynamics of neurons belonging to the ACC-projecting subclass [(R); $n$ = 101 neurons], the EC-projecting subclass [(S); $n$ = 34 neurons], and across the two subclasses [(T); $n$ = 135 neurons, five fields of view, one mouse]. $P$ < 0.0001 (rank sum test computed during epochs of running, against levels estimated from neurons belonging to different fields of view). Shaded areas represent the 95% CI.

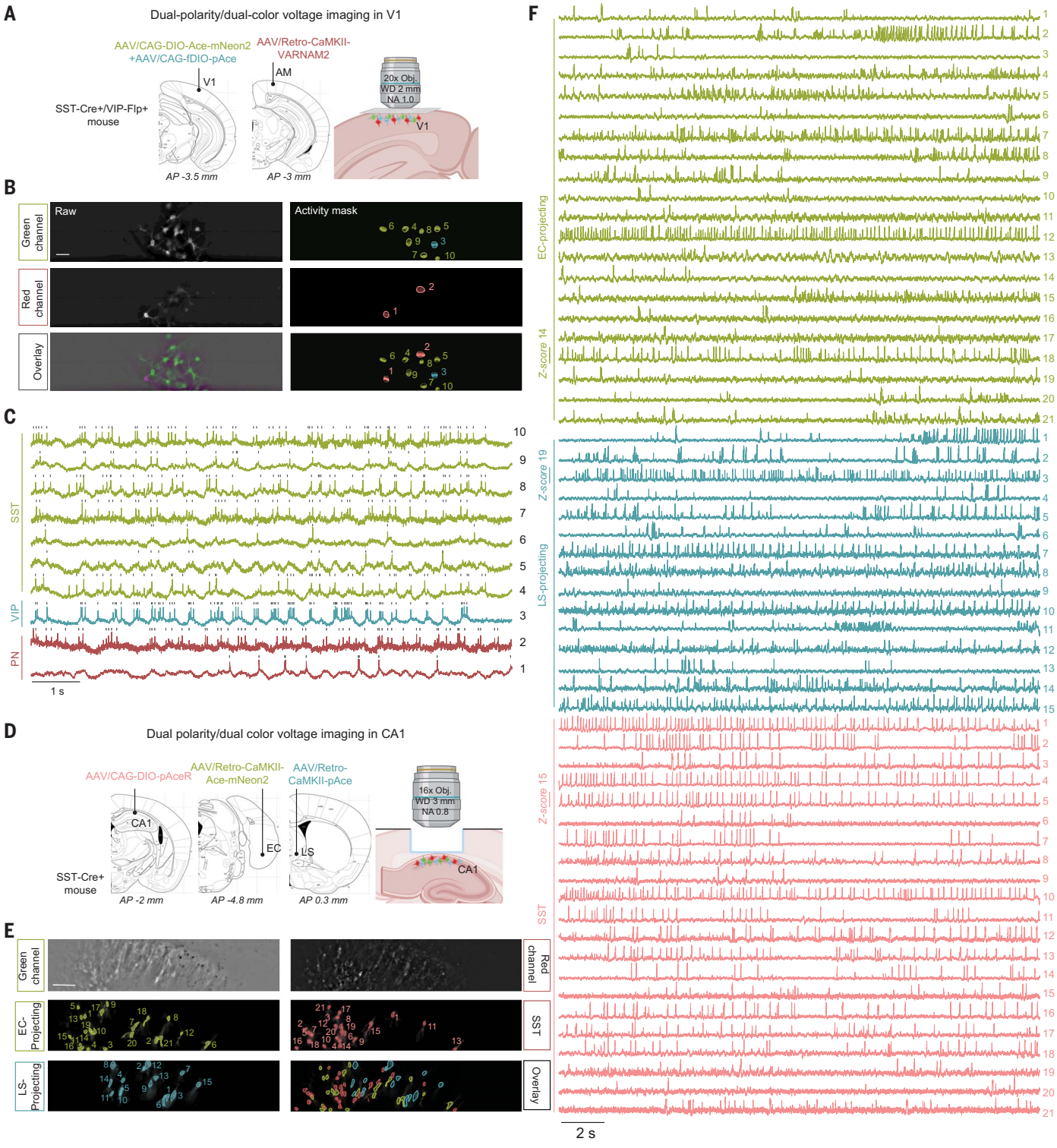


**Fig. 6. Simultaneous dual-polarity and dual-color imaging capture the voltage dynamics of three distinct targeted subtypes or cell subclasses in awake mice.** (**A**) Schematic of AAV injections for three–cell type V1 imaging. (**B**) Raw epifluorescence (left) and activity-mask (right) images of a single field of view in the green and red channels and overlay. Scale bar, 50 μm. (**C**) $\Delta F/F$ traces from the cells numbered in the mask overlay image in (B) and representing $SST^+$ interneurons, $VIP^+$ interneurons, and PNs expressing Ace-mNeon2 (green), pAce (blue), and VARNAM2 (dark red), respectively. Ace-mNeon2 and VARNAM2 traces are inverted for visualization purposes. (**D**) Schematic of AAV injections for three–cell class voltage imaging in CA1. (**E**) Representative field of view of the red and green channels with the respective spatial footprint of the identified neurons belonging to each of the three cell classes. Scale bar, 50 μm. (**F**) $\Delta F/F$ traces for all neurons in (E), representing EC- and LS-projecting excitatory neurons and $SST^+$ interneurons expressing Ace-mNeon2 (green), pAce (blue), and pAceR (light red), respectively. Ace-mNeon2 traces are inverted for visualization purposes.

multiple genetically identified ensembles in awake animals. Notably, our indicators can provide large datasets for quantitative characterizations of the spiking patterns of targeted neuron types in behaving flies and mice. This provides a starting point for future studies in which the fine-scale dynamics between targeted cell types can be examined toward dissecting the circuit basis of animal behavior. The FRET-opsin GEVIs introduced here are bright and can be used with illumination levels far lower than those needed for imaging opsin GEVIs (*16*, *22*, *23*, *27*). They are hence compatible with both widefield epifluorescence microscopy and specialized microscopy methods that use sculpted illumination patterns (*16*, *22*, *24*), facilitating broad dissemination of our voltage imaging approaches.

Our V1 data, acquired from ~1200 cells using Ace-mNeon2, reveal that $SST^+$ interneurons exhibit a major increase in spontaneous firing during arousal, recapitulating the results of targeted patch recordings (*4*). Although our results do not confirm the $VIP^+$ neuron-centered PN disinhibition model (VIP ⊣ SST ⊣ PN), which was proposed based on $Ca^{2+}$ imaging data (*2*, *65*, *66*), the distinct findings might stem from key experimental differences, such as the presence or absence of visual stimuli (*67*). However, past interpretations of $Ca^{2+}$ imaging data might be confounded by subtype-specific differences in intracellular $Ca^{2+}$ dynamics or cytosolic $Ca^{2+}$ release, which in turn may be influenced by state-dependent neuromodulatory effects (*67*). A prior alternative to $Ca^{2+}$ imaging was to perform targeted whole-cell patch electrode recordings, but the invasiveness of the technique and the availability of fewer healthy cells for successful patching makes it challenging to sample large numbers of cells from sparse populations (e.g., $VIP^+$ interneurons) (*2*). The use of GEVIs avoids such limitations of electrodes and $Ca^{2+}$ imaging, and our suite of four compatible GEVIs enables unprecedented studies of spiking in multiple identified neuron classes at once.

Notwithstanding, our imaging methodology does have limitations. Our widefield one-photon epifluorescence imaging studies in the mouse neocortex, like other recent voltage-imaging studies (*13*, *16*, *23*, *24*), were limited to supragranular cortical layers, relatively sparse fluorescence labeling patterns, and moderately sized fields of view. Similarly, our studies of the CA1 hippocampal area were limited to its two most superficial layers. In these regions, by combining high brightness indicators with cell type–specific and soma-targeted labeling strategies, we achieved high signal-to-background fluorescence and exceptional $d'$ values for accurate spike detection and timing estimation (fig. S18), independent of the cell-extraction algorithm used (fig. S15, B, D, and G).

To access cells in deeper cortical layers, the use of patterned illumination strategies to reduce background fluorescence may improve imaging depths (*16*, *22*, *24*, *68*). Alternatively, imaging of voltage dynamics in infragranular cortical layers or deep brain areas with a microprism (*69*) or gradient index (GRIN) microendoscope (*70*) should also be feasible, especially if high numerical aperture lenses (*71*) for enhanced fluorescence collection are used instead of those typically used for $Ca^{2+}$ imaging (*72*). Further, although the densities of labeled cells in our recordings (<370 cells $mm^{-2}$) were comparable to those of past voltage-imaging studies (*13*, *16*, *22*, *23*), they were low compared with the total neuronal density in the mammalian cortex. Thus, our imaging approach may not generalize to studies requiring pan-neuronal or other dense labeling strategies. That said, recent work has aimed to delineate the large number of mammalian neuron types in the cortex (*73*), so we expect that upcoming studies that seek to differentiate the functional attributes of these distinct cell types will require targeted labeling strategies such as those used here. With continued progress in scientific-grade image sensor chips, we also expect improved high-speed cameras that will enable voltage imaging over larger fields of view and of more cells than those studied here.

We quantified the veracity of optically detected spike trains using the $d'$ metric, but measuring the fidelity of optically detected, subthreshold membrane potential changes is more challenging because the relevant fluorescence signals and noise fluctuations are not just frequency-dependent but also nonstationary. Although the subthreshold components of the estimated neural activity traces, $\Delta F/F(t)$, did vary to a modest extent with the use of different cell-extraction algorithms (fig. S15), likely due to different efficacies in computationally removing background fluorescence contaminants or heartbeat artifacts, the biological conclusions obtained about cell class interactions using spike rate correlations and subthreshold correlations were in general agreement with each other (Fig. 3, H to M) and did not depend on the analytic approach to cell extraction (fig. S22). Nonetheless, further progress in cell-extraction algorithms that are tailored for voltage-imaging studies remains important.

Traditionally, multipopulation imaging has been achieved using spectrally orthogonal indicators (*18*, *58*–*61*). Yet, likely due to the limited set of mutually compatible sensors or the need for tailored optical hardware, simultaneous multichannel imaging is not widely performed in live animals. DUPLEX offers a simple alternative to distinguish between two neuron types using one fluorescence channel. Here, DUPLEX unveiled anticorrelated dynamics among pairs of visual cortical $SST^+$ and $VIP^+$ interneurons during arousal. In the hippocampus, DUPLEX revealed cell type–specific subthreshold activity, which allowed us to characterize how the dynamics of excitatory and inhibitory populations relate to those of the LFP. Our results fit with the hypothesis that excitatory neurons contribute more strongly to the LFP because of their spatial organization and temporal synchronization (*74*).

Whereas DUPLEX allows recordings from nonoverlapping cell types, our green and red indicators can be combined for studies of two cell populations that overlap or for which the degree of overlap is unknown. The ACC- and EC-projecting CA1 ensembles represent spatially distinct subpopulations, as seen from the nonoverlapping expression of Ace-mNeon2 and VARNAM2 (Fig. 5M). This anatomical distinction and the separate dynamical attributes of the two cell classes (Fig. 5, P to T) are in line with the idea that there are heterogeneous parallel modules in the hippocampus (*75*).

Looking ahead, that our two green GEVIs of opposite polarities can be further combined with our red GEVIs should enable many different voltage-imaging studies of three or four cell classes simultaneously (Fig. 6). Thus, the new indicators collectively empower neuroscientists to unravel intercellular interactions within and between targeted neuron classes in awake behaving animals.

## Materials and methods

### *Plasmids*

For high-throughput screening in HEK cells, VARNAM and Ace-mNeon were inserted into a modified pCAGGS backbone (*18*). A nuclear localization sequence (NLS)–tagged FP reporter (mCerulean for VARNAM and mCherry for Ace-mNeon) was fused to the C terminus of the indicator interspersed by a T2A ribosomal skipping signal. For in vivo voltage imaging, the indicators were cloned in AAV backbones. pAAV-CaMKII-Ace-mNeon2, pAAV-CaMKII-VARNAM2, and pAAV-CaMKII-pAce were cloned by inserting the respective indicator sequences in place of enhanced green fluorescent protein (EGFP) between the Kpn I and Hind III sites of pAAV-CaMKII-EGFP (Addgene #50469). *Cre*-dependent constructs for Ace-mNeon2 and pAceR were generated by cloning the respective inverted open reading frame (ORF) sequences in pAAV-CAG-Flex-EGFP (Addgene #59331) by replacing the floxed EGFP cassette between the Asc I and Nhe I sites. Likewise, *Flp*-dependent VARNAM2 and pAce constructs were cloned by introducing the respective inverted ORF sequences in place of the floxed mNeonGreen between the Asc I and Nhe I sites in pAAV-CAG-fDIO-mNeonGreen (Addgene #99133). All AAV constructs above included a Golgi–endoplasmic reticulum export sequence and a Kv2.1 proximal restriction and clustering sequence (*43*) at the C terminus of the indicator sequence for

improved membrane trafficking and perisomatic localization, respectively.

### Fly stocks

To create transgenic flies carrying the four improved FRET-opsin GEVIs, we synthesized codon-optimized transcripts for Ace-mNeon2, VARNAM2, pAce, and pAceR using a commercial gene synthesis service (GenScript) and then inserted them in place of green fluorescent protein (GFP) in the *pJFRC7-20×UAS-IVS-mCD8::GFP* (Addgene #26220) and *pJFRC19-13×LexAop2-IVS-myr::GFP* backbones (Addgene #26224). After verifying the sequences of the plasmids, we inserted the plasmids into the attP40 or VK00027 phiC31 docking site to generate *20×UAS-Ace-mNeon2*, *13×LexAop-Ace-mNeon2*, *20×UAS-pAce*, *13×LexAop-pAce*, *20×UAS-VARNAM2*, *13×LexAop-VARNAM2*, *20×UAS-pAceR*, and *13×LexAop-pAceR* flies using a commercial transformation service (Bestgene Inc.).

We obtained MB058B, MB296B, and MB085C split-GAL4 lines from the FlyLight team at Janelia Research Campus and *R82C10-LexA* (#54981) from the Bloomington Stock Center. We raised all flies on standard cornmeal agar media under a 12-hour light-dark cycle at 25°C and 50% relative humidity.

### Site-directed saturation mutagenesis

Mutagenic libraries were generated on Ace-mNeon-T2A-NLS-mCherry and VARNAM-T2A-NLS-mCerulean backbones using a preestablished protocol (*18*). Briefly, a set of four forward primers containing degenerate codons WKC, NMC, VWG, or DGG at the target site was pooled with a single, partially overlapping reverse primer, and mutagenizing polymerase chain reaction (PCR) reactions were set up using CloneAmp polymerase (Clontech). After Dpn I treatment to digest unmutated template, the linear PCR products were circularized using InFusion ligase (Clontech) and transformed in TOP10 competent cells (Invitrogen). To obtain up to 19 unique amino acid substitutions at a single target site, 48 colonies were picked and cultured in 96–deep-well culture plates. Plasmid DNA was isolated using Nucleospin 96 Plasmid kit (Macherey-Nagel) on an epMotion 5075 liquid handling workstation (Eppendorf), and purified DNA was collected in 96-well plates. The libraries were sequenced after voltage screening to identify the individual mutations and ensure that at least 19 variants were obtained at every site.

### Maintenance and transfection of HEK and excitable HEK cells

HEK293 cells (ATCC® CRL-1573™) were maintained in high-glucose Dulbecco's minimum essential medium (DMEM)/10% fetal bovine serum (FBS). Excitable HEK cells (ATCC CRL-3269) (*30*, *31*) were maintained in DMEM/F12, 10% FBS, 1% penicillin (100 U $ml^{-1}$), streptomycin (100 μg $ml^{-1}$), geneticin (500 μg $ml^{-1}$), and puromycin (2 μg $ml^{-1}$) as described previously. About 24 hours before transfection, the cells were plated on poly L-lysine–coated 12-mm coverslips or 96-well glass-bottomed plates in antibiotic-free media. Plasmid DNA (0.5 μg per 12-mm coverslip or 0.2 μg per well of a 96-well plate) was transfected using Lipofectamine (ThermoFisher), and cells were imaged 1 to 2 days after transfection. Both cell lines served solely as a system for the expression and characterization of voltage indicators rather than the subject of investigation.

### High-throughput semi-automated voltage screening

High-throughput voltage screening (Fig. 1B) was performed on a custom-built platform described previously (*18*). A white-light source pE-4000 (CoolLED, UK) was used for sample illumination. For imaging Ace-mNeon, we used a 472/30-nm excitation filter, 495-nm dichroic mirror, and 520/35-nm emission filter (Semrock). For VARNAM and mCherry (reporter fluorophore in Ace-mNeon constructs), we used a 560/40-nm excitation filter, 585-nm dichroic mirror, and 630/75-nm emission filter (Chroma Technologies Corporation). mCerulean reporter in the VARNAM constructs was imaged using a 455/40-nm excitation filter, 458-nm dichroic mirror, and 480/30-nm emission filter (Semrock). After identifying transfected cells in the reporter channel, time-series fluorescence images were captured in the respective GEVI channels using an ORCA Flash4.0 sCMOS camera (Hamamatsu) at 50 Hz. A single pulse of 60 V/0.5 ms was applied using a Grass S48 Stimulator, 1 s after baseline fluorescence acquisition ($F_0$). The percent change in fluorescence at time $t$ was obtained using the formula

$$\frac{\Delta F}{F_0}\% = \frac{F(t) - F_0}{F_0} \times 100$$

Platform automation, sample illumination, data acquisition and parallel data analysis were controlled using custom-written virtual instruments in LabView.

### Fluorescence voltage imaging in cultured HEK cells

Whole-cell voltage-clamp recordings were performed between 22° and 25°C. The bath solution contained (in mM) 125 NaCl, 2 KCl, 10 HEPES, 30 glucose, 3 $CaCl_2$, 1 $MgCl_2$ (~310 mOsm $liter^{-1}$, pH 7.3). The intracellular solution consisted of (in mM) 125 K-gluconate, 8 NaCl, 0.6 $MgCl_2$, 0.1 $CaCl_2$, 1 EGTA, 4 $Mg_2$-ATP, 0.4 Na-GTP, and 10 HEPES. Patch pipettes had tip resistances of 4 to 5 megaohms, yielding series resistances of <20 megaohms. In the voltage-clamp mode, voltage steps in increments of 20 mV/ 0.5 s were applied using a MultiClamp amplifier controlled by pClamp10 software.

Fluorescence recordings were obtained using an Olympus upright microscope. Cells were visualized under a 1.0 NA 60× water-immersion objective lens. Ace-mNeon and pAce were imaged using a 505-nm light-emitting diode (LED) (Thorlabs) and a filter set composed of a 509/22-nm excitation filter, 526-nm dichroic mirror, and 544/24-nm emission filter (Semrock). VARNAM and pAceR were illuminated using a 565-nm LED (Thorlabs), 560/40-nm excitation filter, 585-nm dichroic mirror, and 630/75-nm emission filter (Semrock). The illumination intensity at the sample plane for all indicators was 15 to 20 mW $mm^{-2}$. Fluorescence time-series images (1 to 5 kHz) were captured using a NeuroCCD camera, controlled via NeuroPlex software (RedShirtImaging, GA). Fluorescence response traces were extracted by ranking each pixel by their signal-to-noise ratios, where the noise was calculated as the root mean square value of the baseline fluorescence fluctuations. The top 25% of the SNR-ranked pixels were used to calculate the $\Delta F/F$ values shown in Fig. 1D and fig. S5. Probe kinetics for activation ($\tau_{ON}$) and deactivation ($\tau_{OFF}$) were calculated from 5-kHz recordings obtained in HEK cells, by fitting the first 50 ms of the step responses using a double exponential equation as described previously (*76*).

### Surgical dissection of live flies

We created an optical window on the fly head using an ultraviolet (UV) laser microsurgery system, as described previously (*77*). In brief, we anesthetized the flies by placing them on ice for 1 min and then transferring them to a cooled surface (~4°C) consisting of an aluminum thermoelectric cooling block. We then glued the fly's thorax with a 125-μm-diameter fused silica optical fiber (PLMA-YDF-10/125, Nufern) on a custom-made plastic fixture. To minimize head motion, we glued the fly's head to the thorax using a UV light curing epoxy (NOA 89, Norland). After transferring the mounted fly to the surgery station, we created an optical window in the cuticle by laser-drilling a 150-μm-diameter hole (30 to 40 pulses, delivered at 100 Hz, 36 mJ per pulse, as measured at the specimen plane). Immediately after surgery, we applied 1 ml of UV epoxy (NOA 68, Norland; refractive index: 1.54; transmission 420 to 1000 nm: ~100%) and cured it for ~30 s to seal the cuticle opening.

### Visual cortical surgeries

Animal experiments were performed according to the guidelines of the National Institutes of Health and approved by The John B. Pierce Laboratory Animal Care and Use Committee.

#### Intracranial AAV injections

C57BL/6J wild-type and VIP-*Cre*, SST-*Cre*, VIP-*Flp*, and NDNF-*Cre* transgenic mice were

purchased from The Jackson Laboratory (JAX #664, #31628, #13044, #28578, #28536). NDNF-*Cre*$^{+/+}$ or SST-*Cre*$^{+/+}$ mice were crossed with VIP-*Flp*$^{+/+}$ to generate the NDNF-*Cre*$^{+}$/VIP-*Flp*$^{+}$ and SST-*Cre*$^{+}$/VIP-*Flp*$^{+}$ double driver lines. The following AAV vectors were custom-produced at the University of North Carolina Vector Core at high titers (>1 × $10^{13}$ GC $ml^{-1}$): AAV/DJ-CAG-DIO-Ace-mNeon2, AAV2/Retro-CaMKII-Ace-mNeon2, AAV/DJ-CAG-fDIO-pAce, AAV2/Retro-CaMKII-pAce, AAV/DJ-CAG-fDIO-VARNAM2, AAV2/Retro-CaMKII-VARNAM2, and AAV/DJ-CAG-DIO-pAceR. All AAV vectors above encode soma-targeted versions of the indicators. AAV5-CaMKII-mCherry-*Cre* and AAV2/Retro-EF1A-mCherry-IRES-*Cre* viruses were purchased from the UNC Vector Core and Addgene (#55632), respectively.

Mice were used without regard to sex; we used a total of 21 males and 23 females in this study. Stereotactic AAV injections were performed in 3- to 4-month-old mice under 1.5% (v/v) isoflurane anesthesia. Each animal received five injections in area V1. The coordinates for the V1 injections (Figs. 1, H to K; 2; 3; 5, A to L; and 6, A to C; and figs. S16, S17, S19, and S21) were [in mm from Bregma; (AP, ML, and DV): 2.5, 2.5, and 0.2 (site 1); 2.8, 2.0, and 0.2 (site 2); 3.0, 2.5, and 0.2 (site 3); 3.4, 2.0, and 0.2 (site 4); 3.6, 2.75, and 0.2 (site 5). For PN projection labeling in the anteromedial (AM) visual cortical area (Figs. 1J and 2E and fig. S21), the coordinates were (AP, ML, and DV): 3.0, 0.96, and 0.4. Injections were performed using beveled glass micropipettes delivering a total of 50 to 100 nl virus per site at a rate of 100 nl/min.

For targeted recordings from identified neuron types (Figs. 1, H to K, and 2; and figs. S16, S17, and S19), AAV/DJ-CAG-DIO-Ace-mNeon2 (or AAV/DJ-CAG-fDIO-pAce) was injected in *Cre*- (or *Flp*)-recombinase–expressing transgenic driver lines. For DUPLEX imaging (Figs. 3 and 5, A to L), AAV/DJ-CAG-DIO-Ace-mNeon2 and AAV/DJ-CAG-fDIO-pAce viruses were mixed at a 1:3 (v/v) ratio for injections in NDNF-*Cre*$^{+}$/VIP-*Flp*$^{+}$ or at a 1:1 ratio for injections in SST-*Cre*$^{+}$/VIP-*Flp*$^{+}$ mice. For DUPLEX recordings from PNs with VIP$^{+}$ interneurons in VIP-*Flp*$^{+}$ mice (Figs. 3, L and M, and 5, I to L; and fig. S21), the AAV/DJ-CAG-DIO-Ace-mNeon2 virus was mixed with the AAV5-CaMKII-mCherry-*Cre* virus for Ace-mNeon2-labeling of PNs and injected together with an equal volume of the AAV/DJ-CAG-fDIO-pAce virus for pAce-labeling of VIP$^{+}$ interneurons. To lower PN labeling densities by labeling a subset of neurons projecting to a higher-order visual cortical area (Figs. 1J and 2E), the AAV/DJ-CAG-DIO-Ace-mNeon2 virus was injected locally in V1, whereas the AAV2/Retro-EF1A-mCherry-IRES-*Cre* virus was delivered to the AM cortical area.

For dual-color imaging (Fig. 6, A to C), AAV/DJ-CAG-DIO-Ace-mNeon2 and AAV/DJ-CAG-fDIO-VARNAM2 were mixed at a 1:1 (v/v) ratio for injections in an SST-*Cre*$^{+}$/VIP-*Flp*$^{+}$ background.

### *Histology and confocal imaging*

For confocal imaging of the cell type–specific expression of Ace-mNeon2 in area V1 (Fig. 2, B to E, subpanel a), injected mice were transcardially perfused with ice-cold Sorenson's buffer (pH 7.4) followed by 4% paraformaldehyde. The brains were isolated and post-fixed overnight at 4°C. Forty- to 60-μm-thick coronal sections comprising the visual cortical areas were prepared on a Leica vibratome and mounted on gelatin-coated glass microscope slides using ProlongGold (Invitrogen). Confocal micrographs were obtained using Zeiss LSM 710 under a 20× air objective.

### *Headpost and cranial window implantation*

Headpost and cranial windows were implanted between 25 and 30 days after injection with some modifications to a preestablished protocol (*78*). Mice were anesthetized using a mixture of ketamine (100 mg/kg) and xylazine (16 mg/kg). A custom-designed titanium head post was affixed to the skull using C&B Metabond (Parkell), after which a 3-mm-diameter circular craniotomy was made over the injection area in V1. A sterile double-glass window, assembled by gluing one each of 3-mm- and 5-mm-diameter circular coverslips (Warner), was secured in place using Vetbond, as previously described (*78*). C&B Metabond was applied over the window margins and the remainder of the exposed skull. Carprofen (5 mg/kg, subcutaneously, every 24 hours for 48 hours) and buprenorphine (100 μg/kg, subcutaneously, every 12 hours for 48 hours) were administered as part of postoperative analgesia. Before awake imaging experiments, the headposted mice were handled and habituated to run on a custom wheel every day for up to 2 weeks in 10- to 20-min training sessions. Imaging began once the animal was fully wheel trained.

#### *Hippocampal CA1 surgeries*

The Stanford Administrative Panel on Laboratory Animal Care (APLAC) approved all procedures involving animals, and we complied with all ethical regulations.

### *Hippocampal AAV injections*

C57BL/6J wild-type and SST-*Cre* transgenic mice were purchased from The Jackson Laboratory (JAX #664 and #013044). Mice (aged 8 to 16 weeks at start) underwent two surgical procedures under isoflurane anesthesia (1.5 to 2% in $O_2$). In the first procedure, we injected AAVs to express the fluorescent voltage indicators. In the second procedure, performed about a week after viral injection, we inserted a cannular implant for hippocampal imaging.

The coordinates for CA1 injections in Figs. 4 and 6, D to F, and figs. S23 and S24, were (in mm from Bregma; AP, ML, DV) −1.8, −2.5, −1.1 and −1.3, −1.3, −1.1. The coordinates for retrograde labeling in the lateral septum (LS) (Fig. 6, D to F), entorhinal cortex (EC) (Figs. 5, M to T and 6, D to F; and figs. S23, S24, and S26), and anterior cingulate cortex (ACC) (Fig. 5, M to T; and fig. S26) were, respectively (in mm from Bregma; AP, ML, DV) 0.3, 0.3, −3; −4.8, 3.3, −3.5; and 0.8, 0.2, −1.5. We used the viruses AAV/DJ-CAG-DIO-Ace-mNeon2 and AAV2/Retro-CaMKII-pAce to label SST$^{+}$ neurons and EC-projecting neurons, respectively (Fig. 4); AAV2/Retro-CaMKII-VARNAM2 and AAV2/Retro-CaMKII-Ace-mNeon2 to label EC-projecting and ACC-projecting neurons, respectively (Fig. 5); AAV2/Retro-CaMKII-Ace-mNeon2, AAV2/Retro-CaMKII-pAce, and AAV/DJ-CAG-DIO-pAceR to label EC-projecting and LS-projecting neurons and SST$^{+}$ neurons, respectively (Fig. 6); and AAV/DJ-CAG-DIO-pAceR and AAV2/Retro-CaMKII-VARNAM2 to label SST neurons and EC-projecting neurons, respectively (fig. S23). All viral vectors had titers of >$10^{12}$ genome copies $ml^{-1}$ and were custom produced at the UNC Vector Core.

### *Cannular implant fabrication and preparation of LFP electrodes*

Cannula implants were prepared under a stereomicroscope (Leica MZ7-5) with a fully equipped solder station. The hippocampal cannula consisted of a circular borosilicate cover glass (3 mm in diameter, 170 ± 5 mm thickness, Schott) glued to the end of a 3-mm outer diameter (OD), 1.5-mm-long stainless-steel ring, using UV-curable adhesive (Loctite 3105) (Figs. 5, M to T, and 6; and fig. S23).

For the dual-modality optical-LFP hippocampal recordings (Fig. 4), we affixed three ~1-cm-long, ~50-μm-diameter tungsten wires coated with single polyimide insulation (M215580, California Fine Wire) to the optical cannula at three different axial positions, spaced in increments of ~50 μm. The tip of one of the three tungsten wires was placed flush with the optical window, and the tips of the other two extended beyond the optical window. This set of electrode placements was chosen to maximize the chances that at least one of the electrodes would provide high-quality LFP signals, given that our surgical placement of the implant was performed without fine visual feedback about the exact location of the ~100-μm-thick CA1 pyramidal cell layer. We glued these tungsten wires onto the optical cannula with UV light–cured adhesive, which constrained the electrodes to be laterally offset by 1.5 mm from the center of the imaging window. Next, we soldered a gold-plated pinhead (NC0102069, WPI) onto the end of each tungsten wire projecting away from the imaging window. The reference electrode was

composed of a ~5-mm-long, ~127-μm-diameter, uncoated, stainless-steel wire (#791600, A-M Systems) soldered to a gold-plated pinhead (NC0102069, WPI). Separately, we fabricated a four-channel connector using four gold-plated sockets (NC1456862, WPI) and a connector board (EIB8, Neuralynx).

### *Hippocampal cannular implantation*

To implant the optical cannula, we resected the skin and scalp to expose the dorsal surface of the cranium and removed any remaining connective tissue by cleaning the exposed skull with hydrogen peroxide ($H_2O_2$). To ensure strong adhesion between the cannula implant and the skull, we slightly roughened the skull surface using a drill bit and then rinsed the cranium with Ringer's solution. We drilled a 3-mm-diameter opening above the right dorsal CA1, sized to allow the cannula implant to fit in snugly. We aspirated the cortex above dorsal CA1 using a 30-gauge blunt needle, under irrigation with ice-cold Ringer's solution. We proceeded with cortical aspiration until the light-scattering, myelinated axon bundles of the corpus callosum became visible. Of the three superimposed layers of myelinated axons, which were visually distinguishable by their distinct orientations, we removed the top two layers with gentle air suction, while making sure to leave intact the *stratum oriens* layer of the hippocampus. (We excluded from further study any mice with surgical damage to CA1, because such damage can lead to local epileptiform activity.) The cannula implant was then inserted and affixed to the skull using UV-curable adhesive (Loctite 3105).

For studies in which LFP recordings were to be performed concurrently with imaging, we drilled a 0.5-mm-diameter hole into the skull above the cerebellum, inserted the reference electrode into cerebellar tissue and then affixed it to the skull with UV-curable adhesive (Loctite 3105). Carprofen (5 mg $kg^{-1}$) was administered 30 min before the end of the surgery to mitigate pain. To enable head-fixation during in vivo imaging, we secured a custom stainless steel head bar to the mouse's skull using blue light-cured resin (Flow-it ALC, Pentron). Carprofen (5 mg $kg^{-1}$) was administered up to 2 days after surgery as part of postoperative analgesia. Mice recovered for ~2 weeks before the start of voltage imaging sessions.

### *Voltage imaging in awake flies*

The fly data was acquired at Stanford University. The optical instrumentation described below was used to obtain the data in Fig. 1, E to G; and figs. S13, S14, and S25.

### *Instrumentation and imaging*

To image voltage dynamics in flies, we used a custom-built upright epi-fluorescence microscope and a 1.0 numerical aperture (NA) 20× water-immersion objective (XLUMPlanFL, Olympus). For Ace-mNeon and pAce imaging, we used a 503/20-nm excitation filter (Chroma), 518-nm dichroic (Chroma), and 534/30-nm emission filter (BrightLine). We illuminated the sample using the 500-nm wavelength module of a solid-state light source (Spectra X, Lumencor), with 5 to 7 mW of optical power at the specimen plane. For VARNAM and pAceR imaging, we used a 559/25-nm excitation filter (Semrock), 580-nm dichroic (Chroma), and 630/50-nm emission filter (Semrock). We illuminated the sample using the 550-nm wavelength module of the light source, with 8 to 10 mW of optical power at the specimen plane. We acquired images at 1000 Hz, using a scientific-grade CCD camera (Zyla 4.2, Andor) and 2 pixel–by–2 pixel binning.

### *Odor delivery*

To image odor-evoked activity, we perfused odors to the flies' antennae using a custom-built olfactometer that delivered constant airflow (200 ml $min^{-1}$) to either the control path (mineral oil) or the odor path (odorant dissolved in mineral oil). We presented 5% isoamyl acetate (CAS# 123-92-2, Sigma-Aldrich Inc.), 3% benzaldehyde (CAS# 100-52-7, Sigma-Aldrich Inc.), or apple cider vinegar (Bragg Inc.) to the fly using a probe needle [1.7 mm inner diameter (ID), Grainger Inc.], ~3 mm in front of the antenna. Each odor delivery trial lasted for 5 s.

### *Spike extraction*

To extract the voltage data, we motion-corrected the raw videos using the Turboreg algorithm for image registration (http://bigwww.epfl.ch/thevenaz/turboreg/) (*79*). We then selected pixels whose mean fluorescence intensity, averaged over the entire movie, was in the top 10% of all pixels across the field of view; we defined the union of these high-ranking pixels as the region of interest (ROI). We corrected for photobleaching by fitting a double exponential function to the spatially averaged fluorescence across the ROI, $F(t)$, and then dividing $F(t)$ by the fitted double exponential trace. We then computed time-dependent changes in the relative fluorescence intensity, $\Delta F(t)/F = (F'(t)-F_0)/F_0$, where $F'(t)$ was the time-dependent fluorescence intensity trace across the ROI after the photobleaching correction and $F_0$ was the time-averaged baseline intensity in the ROI after the photobleaching correction. To identify individual spikes, we high-pass filtered the $\Delta F(t)/F$ trace by subtracting a median-filtered (40-ms window) version of the trace and identified spikes as local peaks that surpassed a set threshold (3 SD for PPL1-DANs, 2 SD for MBON-γ1pedc>α/β). We estimated the instantaneous, time-dependent spike rate by tabulating the number of spikes within a 100-ms sliding window.

To determine the mean spike waveform, we averaged the waveforms of all spikes across a trial. We then performed a spline interpolation (10-μs intervals) of the mean waveform and, from the resultant, determined the spike amplitude and duration. Determinations of the spike detection fidelity for studies in live flies were performed using the same formulas as were used for the studies in mice (see section Determinations of the spike detection fidelity index, $d'$).

### *Single- and dual-channel voltage imaging in V1 in running mice*

All data from brain area V1 (Figs. 1, H to K; 2, B to E; 3; 5, A to L; and 6, A to C; and figs. S16, S17, S19, S21, and S22) were acquired at the John B. Pierce Laboratory. Before the awake animal experiments, head-posted mice were handled and acclimated to a custom 15-cm-diameter 3D-printed wheel for ~2 weeks in training sessions of 10 min per day.

### *Instrumentation and imaging*

For in vivo neocortical voltage imaging, mice implanted with cranial windows were head-fixed by securing the head post to two points on the custom wheel with thumbscrews. Neurons expressing soma-targeted indicators at cortical depths of ~50 to 200 mm below the pial surface (Fig. 2, B to E, subpanel a) were imaged on a custom-built dual-channel upright fluorescence microscope equipped with an epi-illuminator module (WFA2001, Thorlabs), an EYFP/mCherry (59026, Chroma) dual-bandpass filter set (comprising a 59026× excitation filter with passbands of 503/12 and 575/15, a 69008bs dichroic mirror with passbands of 470/20, 540/25 and 630/50, and a 59026m emission filter with passbands of 535/15 and 635/35), and a 20X 1.0 NA Olympus XLUMPLFLN water immersion objective.

The illumination from a pair of LEDs, emitting light of 505- and 565-nm wavelengths (M505L4 and M565L3, Thorlabs, respectively), was collimated with a pair of aspheric condenser lenses (ACL2520U-A), one for each LED. For dual-channel imaging (Fig. 6, A to C), illumination from the two LEDs was combined using a 550-nm long-pass dichroic mirror (T550 LPXR, Chroma). The illumination intensity at the sample plane in each of the red and green channels was ~25 mW $mm^{-2}$.

Fluorescence emissions returning from the sample plane were directed by a 585-nm long-pass dichroic mirror (T585 LPXR, Chroma) into the two fluorescence detection arms of the microscope. Emissions from Ace-mNeon2 and/or pAce passed through a 520/35-nm bandpass filter (FF01-520/35-25, Semrock). Emissions from VARNAM2 and/or pAceR passed through a 630/75-bandpass filter (ET630/75m, Chroma). Within each fluorescence detection arm, a 0.75× camera tube lens (WFA4101, Thorlabs) focused the fluorescence onto a high-speed sCMOS camera (Orca Flash 4.0 v3, Hamamatsu).

For the dual-color, dual-polarity imaging studies of V1 using Ace-mNeon2, pAce, and VARNAM2 in Fig. 6, A to C, both the 505- and 565-nm LEDs were ON concurrently, and we acquired data simultaneously from both cameras. For synchronized registration of the images, the two cameras were operated in their external trigger mode, allowing us to trigger image acquisition on both cameras by sending them a single, common transistor-transistor logic (TTL) pulse. We further verified that image acquisition by the two cameras was synchronized by using the time stamps on the two videos. To ensure that images from the two channels were spatially aligned, we calibrated images against an alignment target and confirmed this during each imaging session based on reference points, e.g., the location of landmark vasculature.

For all experiments in Figs. 1, H to K; 2, B to E; 3; 5, A to L; and 6, A to C; and figs. S16, S17, S19, S21, and S22, fluorescence time-series images (2048 pixels by 512 pixels) were collected at 400 Hz with 4-by-4 binning. We typically acquired 3 or 4 trials of data from each imaging field of view, and we imaged ~6 to 8 fields of view per session. Over the course of several days, but in some cases over 3 to 4 weeks, we revisited and reimaged each field of view two or three more times, using vascular landmarks to identify the approximate tissue locations of prior imaging sessions.

We inferred the cortical depth of the imaged neurons based on the laminar organization, as reported in the published scientific literature, of the different cortical cell types that we examined. Specifically, we inferred that we recorded neurons in cortical layers 1, 2, and 3 based on published evidence that (i) cortical NDNF$^+$ interneurons are layer 1 specific (*41*, *47*, *48*) and that (ii) cortical PNs, selectively targeted using CaMKII, and SST$^+$ interneurons, selectively targeted using the published SST-*Cre* transgenic line (*40*) are both absent in cortical layer 1. PN projection neurons from the AM area reside in cortical layer 2/3, between 100 and 200 μm below the pial surface (*39*, *42*). SST$^+$ interneurons reside at depths >200 μm beneath the pial surface (*40*), and VIP$^+$ interneurons reside at depths >50 to 100 μm below the pia (*49*). Confocal micrographs showing cell subtype–specific labeling in V1 (Fig. 2, B to E, subpanel a) further confirmed the laminar organization of the imaged cortical cell classes in the supragranular layers and the relative cortical depths of the distinct neocortical subclasses.

### *Visual stimulus presentations*

In Fig. 1J, visual stimuli were generated using the Psychophysics toolbox on MATLAB and were presented to awake, stationary mice on an LCD video monitor (1280 pixels by 1024 pixels, 20 inches by 16 inches, 60-Hz refresh rate, mean luminance of 250 cd m$^{-2}$). The monitor was placed ~15 cm from the animal, perpendicular to the surface of the right eye (contralateral to the injection area). To map the receptive field of an imaged neuron, static bright and dark stimuli were presented individually in a pseudorandom sequence within each square of a 3-by-4 grid extending across the entire video monitor. Once the cell's receptive field location was approximately mapped, to characterize the cell's orientation-selective responses, we sequentially presented a set of drifting sinusoidal gratings at one of eight orientations, spaced by increments of 45° and presented in a pseudorandom sequence. The spatial frequency of the grating was 0.04 cycles per division, and the temporal frequency was 2 Hz. Each trial lasted 16 s, with interstimulus intervals of 500 ms.

### *Induced state transitions and pupillometry*

In Figs. 2, B to E, and 5, A to L, to induce a change of state, a brief 50-ms air puff was delivered to mice at rest using a small tube aimed at the back of the animal. Wheel position was tracked using a programmable angle sensor (KMA210, Digikey). A data acquisition device (NI USB-6259, National Instruments) registered the wheel's position and delivered TTL pulses to initiate image acquisition. Software code that was custom written in LabView 2019 (National Instruments) controlled data acquisition.

For the state-transition experiments in Figs. 2, B to E, and 5, A to L, an infrared camera (Basler A602f) was used to measure the pupil diameter at a frame rate of 15 Hz. Pupil diameter was measured in real time using custom code written in LabView. An annulus region of interest was drawn over the pupil, with the inner circle located at the center of the eye and the outer circle extending past the edge of the pupil. The edge-detection functionality of the LabView Vision Development Module was used to detect dark-to-light transition points along a set of radial measurement lines drawn from the inner circle and extending to the outer circle. The pupil diameter was calculated by fitting a circle to the set of detected dark-to-light transition points. The threshold level for edge detection and the number of transition points were manually optimized for each individual mouse.

### *Single- and dual-channel voltage recordings in CA1 in running mice*

All imaging studies of hippocampal area CA1 were performed at Stanford University. The optical instrumentation described below was used to acquire the CA1 data shown in Figs. 4; 5, M to T; and 6, D to F; and figs. S23, S24, and S26.

### *Instrumentation and imaging*

For green DUPLEX studies (Fig. 4), simultaneous dual-color (Fig. 5, M to T; and figs. S24 and S26), and triple-population voltage imaging (Fig. 6, D to F), we used a custom-built microscope with a 16× 0.80 NA, 3.0-mm working distance (WD), water immersion objective lens (Nikon N16XLWD-PF). For red-DUPLEX (fig. S23), we used a 25× 1.0 NA, 4.0-mm WD, water immersion lens (Olympus XLPLN25XSVMP2). The recording depth for all hippocampal data was ~50 to 100 μm, as set by the intrinsic cellular organization of the dorsal CA1 area. A motorized stage (Sutter MP-285) was used for fine axial focusing.

Illumination from two LEDs (UHP-F-470 and UHP-F-545, Prizmatix) was combined using a long-pass dichroic mirror (511 nm, Prizmatix) and then filtered using a dual-bandpass clean-up filter (Semrock, FF01-482/563-25, with passbands of 482/18 and 563/9 nm). A dual-band dichroic mirror (Semrock, Di01-R488/561-25x36, with passbands of 525/40 and 690/108 nm) reflected the combined illumination toward the specimen and transmitted the returning fluorescence emissions. The illumination intensity at the sample plane from each LED was ~25 to 75 mW mm$^{-2}$.

In the emission pathway, to separate fluorescence in the two color channels, we used a 550-nm short-pass dichroic mirror (70 mm by 100 mm, custom designed, Alluxa) and a pair of emission filters, each of which was specific for one of the two color channels: 520/41 nm (70-mm diameter, custom designed, Alluxa) for Ace-mNeon2 and pAce and 609/62 nm (Semrock, FF01-609/62-50) for VARNAM2 and pAceR.

Each arm of the fluorescence collection pathway was composed of a tube lens of 85-mm effective focal length (Canon, EF 85 mm f/1.2L II USM) and a high-speed scientific-grade CMOS camera (Hamamatsu ORCA Fusion Digital CMOS camera; Hamamatsu Photonics K.K., C14440-20UP). Data acquisition was controlled by custom software with a field programmable gate array (FPGA)–based (Xilinx Z-7010) back end and a front end written in LabView 64-bit 2019 (National Instruments). Note that although our labs were acquainted with and therefore used LabView to implement the hardware control, other programming languages (e.g., C++, MATLAB, Python) can also be used to control data acquisition if the camera manufacturer provides an appropriate software development package.

As with dual-channel imaging in V1, dual-channel imaging in CA1 (Figs. 5, M to T, and 6, D to F) was performed with both the 470- and 545-nm illumination sources turned ON (or OFF) simultaneously at the beginning (or end) of each trial. Frame acquisitions were synchronized across the two cameras using an external electronic trigger generated by the FPGA. We achieved subpixel spatial alignment between the fields of view of the two cameras by registering them with an alignment target. We verified proper registration using image landmarks, e.g., large blood vessels.

Images were collected at 600 Hz with no spatial binning. Live data from each camera were stored as native DCAM image files (.dcimg) on two separate 2-TB SSD drives. The data were batch-processed offline using the custom pipeline SpikeImagingAnalysis (see section Data extraction pipeline and downstream analyses of hippocampal CA1 datasets for details), which we wrote in MATLAB (Mathworks).

### *Rest-to-run state transition*

For the studies in Fig. 5, M to T, we used a mouse's running wheel (8 cm wide, 13 cm in diameter) that was 3D-printed in PLA plastic. The wheel surface was covered with a self-adherent wrap (Coban, 3M). Angular displacements of the wheel were tracked using a rotary encoder (Optical AB Phase Quadrature Encoder 600P/R, Amazon). A data acquisition interface (BNC-2090A, National Instruments) controlled from LabView was used to acquire the wheel displacement data.

Mice were habituated on the wheel for at least 2 days, for at least 15 min per day, before brain-imaging sessions began. To trigger rest-to-run behavioral state transitions, a brief air puff was delivered to the mouse's back. The air puff intensity was ~30 psi and was administered with a 20-gauge blunt needle placed 1 to 2 cm away from the mouse. For each field-of-view, we performed high-speed voltage imaging across a 30-s trial (18,000 frames at 600 Hz), starting with the mouse at rest. Within each trial, a TTL signal (five pulses at 5 Hz) triggered the air puff delivery after 10 or more seconds of baseline data had been acquired. Each experimental session involved imaging six fields of view, with one air-puff trial per field of view.

### *LFP recordings*

We amplified the electrophysiological signals using a digital recording head-stage (RHD 16-Channel, Part #C3334, Intantech) that was attached to our custom-designed connector. We then acquired the digital data at a sampling rate of 2 kHz using a USB data acquisition board (RHD USB interface board, Part #C3100, Intantech).

To synchronize the optical and electrical recording instruments, we generated a synchronizing digital signal (hereafter called "syncTTL"), which was composed of a square wave signal with a 50% duty ratio and a 1-s-long on-state but with intervals of random duration between pulses, to enable unambiguous temporal alignments. The syncTTL signal was externally and independently generated by a data acquisition system (USB-6003, National Instruments) and was recorded concurrently by both the electrical and the optical data acquisition systems (at 600 Hz and 2 kHz, respectively).

To temporally align the optical and electrical physiological signals (recorded at 600 Hz and 2 kHz, respectively), we first bandpass-filtered the LFP traces (the filter's 3-dB high-frequency cutoff was 500 Hz and the 3-dB low-frequency cutoff was 0.1 Hz). Then, we interpolated the LFP traces and the squared syncTTL signal so that the sampling rates of the resulting traces matched the 600-Hz sampling frequency of the optical data. We used the MATLAB function *interp1* with the "spline" method to interpolate the continuously valued LFP trace. To interpolate the binary- valued syncTTL signal, we used the *interp1* function with the "nearest" method. Finally, we temporally aligned the optical and electrical traces according to the temporal registration provided by the paired set of syncTTL recordings.

### *Data extraction pipeline and downstream analyses of V1 datasets*

Extraction of individual neurons and their fluorescence activity traces for imaging studies in area V1 (Figs. 1, H to K; 2; 3; 5, A to L; and 6, A to C; and figs. S15 and S17 to S22) was performed at the John B. Pierce Laboratory using the open-access Python-based automated pipeline VolPy (*44*), which consisted of the following steps:

1) File loading. We modified the VolPy code to support the .dcimg file format of the data taken with the Hamamatsu camera.

2) Motion correction. Each movie was motion-corrected using the NoRMCorre algorithm (*80*), which is built into the VolPy pipeline.

3) Cell segmentation. Steps 3 and 4 are included as part of the updated SpikePursuit algorithm (*13*) that is built into the VolPy pipeline (*44*) for spike extraction and denoising. Whereas the original version of SpikePursuit used manual input parameters to identify the location of each neuron (*13*), in the updated version, neuron identification and segmentation are performed automatically using a convolutional neural net known as "Mask R-CNN" (*81*), which provides binary masks covering each identified cell.

4) Trace denoising and spike extraction. Fluorescence activity traces are extracted from the regions of the movie covered by spatial masks (ROIs) from step 3. and are then corrected for photobleaching using a high-pass filter (third-order Butterworth filter, 1/3 Hz cut-off). For each ROI, the following two steps are then executed in a loop for three iterations. The first step estimates spike times and the second refines the spatial filter. (Step 1) To estimate spike times, the first eight principal components of background pixels (at >12 pixels from the ROI) are extracted and removed from the fluorescence movie using ridge regression. The resulting trace of fluorescence activity within the ROI after background removal is then high-pass-filtered (fifth-order Butterworth filter, 1 Hz cut-off) to obtain a trace, $t_s$, that contains activity at frequencies typical of neural oscillations and spikes. Spikes are identified as threshold crossing events, and the spike waveforms are averaged to obtain a spike template. A matched filter (*82*) is then derived from this spike template and from additive white Gaussian noise, with the goal of identifying a template waveform that can be applied to a noisy signal. To denoise traces, the matched filter is applied to $t_s$ and spikes are detected again. Lastly, the reconstructed fluorescence trace representing the spike train $t_{rec}$ is obtained by convolving the spike template and the inferred spike train. (Step 2) To refine each cell's spatial mask, its reconstructed trace $t_{rec}$, is regressed onto the fluorescence movie using ridge regression.

### *Automated assignment of cell classes in DUPLEX recordings*

To identify the polarity of the neural spike waveforms in DUPLEX recordings (Figs. 3; 5, A to L; and 6, A to C; and figs. S20 to S22), for each cell, we identified putative spikes in the $t_{rec}$ trace as negative- or positive-going that deviated >3 SD from baseline noise levels. We identified the polarity of the indicator expressed in the cell according to whether it exhibited more negative- or positive-going events (fig. S20). Because VolPy extracts action potentials (APs) through template-matching (*44*), only typical AP waveforms were considered during polarity assignment. Traces with no spikes were not assigned and were removed manually from downstream analyses (see analysis pipeline, fig. S20).

### *Spike rate, spike modulation index, and correlational analyses*

We exported data from VolPy as MATLAB files for downstream analyses. Each cell's firing rate (FR) was estimated by sliding a rectangular window (of 100 ms for Fig. 2 and fig. S19 or 20 ms for Figs. 3, H to M, and 5, C, G, and K; and fig. S17) along the spike train followed by smoothing with a Gaussian kernel of 100 ms using the *smooth* function in MATLAB. The air puff–induced spike modulation indices in Fig. 2, B to E (subpanel d) and 5, D, H, and L; and fig. S19 were calculated as $(FR_{arousal} - FR_{baseline})/(FR_{arousal} + FR_{baseline})$, where FR is the mean firing rate over a 750-ms time window that was either before or after the air puff. In Fig. 2, B to E (subpanels c and d), we temporally aligned the spike rates to the air-puff onset. Pairwise correlation coefficients and cross-correlation values in Figs. 2, F to I; 3, H to M; and 5, C, G, and K; and figs. S17, S21, and S22 were calculated using the *corrcoef* and *xcorr* functions in MATLAB.

### *Data extraction pipeline and downstream analyses of hippocampal CA1 datasets*

Trace extraction for the hippocampal data (Figs. 4; 5, M to T; and 6, D to F; and figs. S18, S23, S24, and S26) was performed at Stanford University using a custom pipeline written in

MATLAB (SpikeImagingAnalysis, https://github.com/sihaziza/SpikeImagingAnalysis_public). This pipeline consisted of the following steps:

1) File loading and motion correction. Raw 16-bit .dcimg video files from voltage-imaging sessions were loaded into memory, underwent spatial (2 by 2) binning, and saved in .h5 data format. Movies underwent motion-correction using NoRMCorre (*79*) and were then cropped so as to remove parts of the images that did not contain fluorescently labeled brain tissue. The NoRMcorre parameter shift_method was set to "cubic," instead of the default "fft."

2) Detrending. To account for fluorescence photobleaching, at each time point in the fluorescence video, $F(t)$, we normalized each pixel by $F_0(t)$, the time-varying value of the pixel's baseline fluorescence, which we computed using a temporal low-pass filter (fourth-order Butterworth filter, 0.5-Hz cut-off frequency). The resultant is the detrended movie, $F(t)/F_0(t)$.

3) Cell extraction. We extracted individual neurons and their time traces of membrane voltage activity using the automated cell-extraction algorithm EXTRACT (*45*, *46*). EXTRACT is generally agnostic about cells' morphologies and activity patterns and therefore has broad applicability to both one- and two-photon fluorescence imaging studies of neural activity. It is based on the mathematical framework of robust statistics, which generally allows it to surpass other widely used cell-extractions algorithms, such as CNMF (*83*) and PCA/ICA (*84*), in the removal of background fluorescence contaminants and cross-talk between overlapping cells (*46*).

In brief, EXTRACT is designed to automatically identify each neuron's spatial profile, S, and retrieve its activity trace, T, using an iterative process that is applied to individual cells, one at a time. This "cell finding" process is followed by an iterative "cell refinement" process.

During cell finding, EXTRACT finds a seed pixel that attains the movie's maximum fluorescence intensity and initializes a candidate cell image at that pixel. The estimates of S and T are iteratively updated in an alternating manner by using a robust regression at each step and a one-sided Huber loss function (*46*). Once the estimates of S and T stabilize for an individual cell, the cell's inferred fluorescence contribution is subtracted from the movie, and the entire set of steps is repeated for another cell. This process continues until no more putative cells are found, which is determined to occur when the peak value for the activity trace of the seed pixel falls below a predefined threshold value (>3× SD of background noise).

During the iterative process of "cell refinement," at each iteration, the set of estimated traces {T} is updated using robust estimation while holding fixed the set of cells' spatial profiles. Next, the spatial profiles {S} are updated using robust estimation while holding fixed the activity traces, {T}. A validation procedure then checks each putative cell against a set of predetermined quality metrics and removes any cell with metrics below predetermined threshold values. This three-step process runs for a fixed number of iterations, and EXTRACT outputs the final estimates of each cell's spatial profile and activity trace.

For DUPLEX studies that involved a pair of similarly colored GEVIs but with opposite polarities, we ran EXTRACT twice: once on the detrended video, $F(t)/F_0$, to identify active neurons expressing the positive polarity indicator, and once on a sign-inverted version of the detrended video, $F(t)/F_0$, to identify active neurons expressing the negative polarity indicator.

4) Spike timing estimation. To precisely estimate each cell's spike train based on its fluorescence activity trace, we used the statistical method MLspike (*85*), which outputs the spike train that is most likely to have led to the observed fluorescence trace. The algorithm requires five input parameters: the saturation S, single-spike amplitude A, single-spike time constant $\tau$, baseline fluctuation "drift," and noise level $\sigma$. The saturation parameter, defined as the number of spikes at which the indicator provides a full-amplitude response, was set at S = 1. We estimated A and $\tau$ using a double-exponential fit to the mean spike waveform, which we computed using only temporally isolated spikes. We empirically estimated the parameter, "drift," by computing peak-to-peak amplitude variation of a low-pass-filtered (fourth-order Butterworth filter, 50-Hz cut-off frequency) version of the cell's activity trace that retained subthreshold activity up to the gamma frequency band but not spiking activity. $\sigma$ was estimated as the standard deviation of the residual signal, defined as the difference between the raw and a denoised version of the cell's fluorescence activity trace (we obtained by applying a wavelet denoising of degree one).

### Computations of oscillatory phase

In Fig. 4, G and H, to calculate the phase of spiking with respect to theta oscillations (5 to 10 Hz), we first band-pass-filtered both the optical voltage trace and the LFP trace at the theta frequencies using the *butter* and *filtfilt* MATLAB functions (fourth-order Butterworth filter, cut-off frequency of 5 to 10 Hz). We then computed the phase of each filtered trace by performing a Hilbert transform (*hilbert* and *angle* functions). For Fig. 4G, we calculated the timing of each spike relative to the period of that oscillation cycle (in degrees). For each cell, we then computed the circular mean to generate Fig. 4H.

### Spike-rate analyses

In Fig. 5, O to Q, all traces (spike rasters and speed traces) were temporally aligned to the rest-to-run transition, which we detected as a discrete change in the running speed (thresholded at >2 cm $s^{-1}$). We then computed the cells' time-varying spiking rates using a 100-ms sliding window. For each neuron type studied, we averaged the time-varying spike rate across all cells to determine the mean spike rate (Fig. 5P). To assess the rest-to-run fold change in instantaneous spiking rates (Fig. 5Q), we computed the spiking rate in the 2-s intervals immediately before and immediately after the state transition.

### Analyses of subthreshold activity

In Fig. 5, R to T, neuronal traces from all fields of view were temporally aligned to the rest-to-run transition. To compute coherence of subthreshold activity between pairs of cells, in either the running or resting states, we first estimated the subthreshold dynamics of each cell by computing low-pass filtered versions (fourth-order Butterworth low-pass filter, cut-off frequency of 50 Hz) of the "drift" output of ML spike for each cell. Next, we computed the magnitude-squared coherence between the two low-pass-filtered time traces by using the MATLAB function *mscohere*, which we applied to 1-s-long segments of data, chosen such that temporally successive segments from the traces overlapped by 0.8 s. To estimate the noise level in such computations, we computed the pairwise coherence of cells belonging to two separate fields of view. In Fig. 4, I to L, we computed the neuron-LFP coherence in a pairwise manner, between the subthreshold activity of each cell and the LFP, determined in the same way as for cell pairs in Fig. 5.

### Comparisons of cell-extraction methods

We compared the results from VolPy and EXTRACT to a simple ROI-based approach for cell extraction. For this comparison, we used DUPLEX data providing joint recordings of $NDNF^+$ and $VIP^+$ interneurons in V1 (Fig. 3, B and C; and fig. S15).

Unlike ROI-based cell extraction, both VolPy and EXTRACT performed comparably in terms of removal of cellular cross-talk (fig. S15, A to H), neuropil contamination (fig. S15, I to N), and hemodynamic artifacts (fig. S15, O to T). Moreover, the inferred biological conclusions were independent of the algorithm used, in that the results obtained using both VolPy and EXTRACT were identical and indicated positively correlated activity within each interneuronal population but no significant correlation of the voltage signals between $NDNF^+$ and $VIP^+$ interneurons (fig. S15, F to H). However, traces extracted using an ROI-based approach showed spurious pairwise correlated activity, suggestive of increased cellular cross-talk, and the presence of hemodynamic artifacts in the subthreshold traces. In addition, the data obtained from ROI-extracted traces were

inconsistent with prior observations as they showed highly positively correlated activity not only within populations but also anomalously between NDNF$^+$ and VIP$^+$ interneurons (*47*, *48*).

### Computations of GEVI impulse responses

In fig. S12, activation and deactivation kernels for each GEVI were determined using a biexponential function from the empirically measured values of each indicator's fast and slow time constants and the relative amplitudes of the fast and slow relaxation processes associated with the indicator's activation and deactivation responses. The empirical values used and the publications from which they are taken are indicated in the caption for table S1.

We determined each GEVI's impulse response function (fig. S12, A and B) by convolving its activation kernel with the rising edge of a 1-ms-duration square voltage pulse (+100-mV depolarization, starting from −70 mV) and its deactivation kernel with the falling edge of the square pulse, and then summing the two resultants at a sampling rate of 5 kHz. To isolate the kinetic aspects of the indicator response, we defined the excursion rate (fig. S12A) as the time-dependent fluorescence emission rate response to the 100-mV voltage pulse, normalized by the indicator's steady-state fluorescence emission rate in response to a maintained 100-mV depolarization (i.e., a 100-mV step function). To account for the different response amplitudes of different GEVIs, we performed the same calculation for each GEVI but without normalizing by the steady-state response amplitude; the resulting plots, termed the "effective 1× AP-$\Delta F/F$" plots (fig. S12B), show each indicator's estimated response to a 1-ms action potential of 100-mV amplitude. To evaluate how different GEVIs respond to a burst of action potentials in quick succession (fig. S12C), we computed indicator responses to a set of three spikes, with each spike modeled as a 1-ms-duration square pulse of 100-mV depolarization, and with the spikes spaced in 3-ms increments. To assess the capability to resolve action potential bursts under typical imaging conditions, we then down-sampled the computed traces to 1 kHz (fig. S12C).

### Determinations of the spike detection fidelity index, d′

To compute $d'$, we used a signal detection theory framework that accounts for both the duration and intensity of fluorescence waveforms in optical recordings of action potentials and that characterizes the ability to correctly distinguish instances of a spike from background noise fluctuations within the fluorescence trace (*17*, *38*). As described in our prior work (*38*), if we use $N$ successive samples from a fluorescence detector, $F = (F_1, F_2, \ldots, F_N)$, to detect spikes, the distribution of $F$ follows Poisson statistics in the shot-noise-limited regime. Given a specific observation, $F$, the Poisson distribution of $F$ enables one to estimate the a posteriori likelihood of two mutually exclusive hypotheses: the null hypothesis, $H^{(0)}$, which posits the absence of a spike; and the alternative, $H^{(1)}$, which posits that a spike occurred. $d'$ can then be calculated as

$$d' = \left(\mu_L^{(1)} - \mu_L^{(0)}\right)/\sigma_L \quad (1)$$

in which $\mu_L$ and $\sigma_L$ respectively represent the mean and variance of the (approximately normal) probability distributions of the log-likelihood ratio, $L(f)$, of the two hypotheses, in the cases when there actually is or is not a spike. The mean, $\mu_L$, and variance, $\sigma_L$, of these log-likelihood ratio distributions are given by

$$\mu_L^{(0)} = \frac{F_0}{\nu}\sum_{n=1}^{N}\log(1+s_n) - \frac{F_0}{\nu}\sum_{n=1}^{N}s_n \quad (2)$$

$$\mu_L^{(1)} = \frac{F_0}{\nu}\sum_{n=1}^{N}(1+s_n)\log(1+s_n) - \frac{F_0}{\nu}\sum_{n=1}^{N}s_n \quad (3)$$

$$\sigma_L \approx \sigma_L^{(1)} \approx \sigma_L^{(0)} = \sqrt{\frac{F_0}{\nu}\sum_{n=1}^{N}\log^2(1+s_n)} \quad (4)$$

Where $\nu$ is the sampling rate, $F_0$ represents the baseline fluorescence intensity in time periods that contain no neural spike, and $s_n$ is the mean fluorescence signal at each time bin within a time period that contains the optical waveform of the identified spikes for each neuron. For studies in flies (figs. S13 and S14C), we determined each neuron's $d'$ value by first computing its mean spike waveform, $s_n$, over an interval of [−25 ms, +25 ms] relative to the spike occurrence time, and then using Eq. 1 to 4 to compute $d'$.

For studies in mice (figs. S16, F and H; and S18), we first used Eq. 1 to 4 to compute a $d'$ value for each action potential fired by an individual cell and then determined the mean $d'$ value averaged across all spikes in the cell's spike train. We used only spikes that were temporally separated from other action potentials by >10 ms, so as to avoid computational biases that could be introduced by spike bursts, e.g., by instances when a cell does not return to its resting membrane potential between spikes. For each isolated spike, we estimated $d'$ using data within a time interval of [−10 ms, +20 ms] relative to the spike's occurrence time.

To determine how the spike detection error rate depended on the imaging frame rate (fig. S18, A and B), we treated the case in which the decision boundary for classifying instances of $H^{(0)}$ and $H^{(1)}$ was set midway between the two log-likelihood probability distributions [see, e.g., figure 1 of (*38*)]. In other words, false-negative and false-positive spikes were considered equally deleterious. When there are abundant fluorescence photons, the two log-likelihood distributions are each approximately Gaussian, with means that differ by $d'$ in units of $\sigma_L$. We used the complementary error function *erfc* in MATLAB to compute the proportion of the area under each log-likelihood probability distribution that was on the opposite side of the decision boundary from the mean of the distribution [i.e., the proportion of cases representing spike detection errors; see figure 1 of (*38*)].

### Statistics

For both the V1 and CA1 datasets, we performed statistical tests using standard MATLAB functions or built-in tests in Prism 8 (GraphPad). For two-sample comparisons of a single variable, we always used nonparametric tests, as described in this section.

In Fig. 1D, to test for significant differences in the mean $\Delta F/F$ values of the indicators, we used Mann-Whitney test. In Figs. 2, F to I, and 5, C, G, and K, for comparisons of pairwise correlation coefficients of spike rates for time bins before versus after air puff, we performed Wilcoxon matched-pairs signed rank test. In Fig. 3, I, K, and M, to assess whether neuron pairs exhibited positively versus negatively correlated activity, we compared the mean pairwise correlation coefficients to zero using one-sample Wilcoxon test. In Fig. 4H, to assess statistical differences in the polar plots, we computed the mean and standard deviation of each data distribution and made statistical comparisons between different distributions using circular statistics. Specifically, we used the Hodges-Ajne test to test the hypothesis of nonuniformity of circular data and the Watson-Williams multisample test to test the hypothesis of equal means. In Fig. 5, D, H, and L, to assess whether neuronal spike rates were positively versus negatively modulated by the air puff, we tested whether mean spike modulation indices were significantly different from zero using a one-sample Wilcoxon test.

We did not use power analysis or statistical methods to estimate sample sizes but instead estimated useful sample sizes based on published reports and our prior experiences with voltage imaging. Data exclusion criteria were not preestablished. However, recordings with no spiking neurons were excluded.

### REFERENCES AND NOTES

1. K. A. Ferguson, J. A. Cardin, Mechanisms underlying gain modulation in the cortex. *Nat. Rev. Neurosci.* **21**, 80–92 (2020). doi: 10.1038/s41583-019-0253-y; pmid: 31911627

2. Y. Fu *et al*., A cortical circuit for gain control by behavioral state. *Cell* **156**, 1139–1152 (2014). doi: 10.1016/j.cell.2014.01.050; pmid: 24630718
3. C. C. Y. Lee, E. Kheradpezhouh, M. E. Diamond, E. Arabzadeh, State-dependent changes in perception and coding in the mouse somatosensory cortex. *Cell Rep.* **32**, 108197 (2020). doi: 10.1016/j.celrep.2020.108197; pmid: 32997984
4. P.-O. Polack, J. Friedman, P. Golshani, Cellular mechanisms of brain state-dependent gain modulation in visual cortex. *Nat. Neurosci.* **16**, 1331–1339 (2013). doi: 10.1038/nn.3464; pmid: 23872595
5. J. Schiemann *et al*., Cellular mechanisms underlying behavioral state-dependent bidirectional modulation of motor cortex output. *Cell Rep.* **11**, 1319–1330 (2015). doi: 10.1016/j.celrep.2015.04.042; pmid: 25981037
6. B. K. Hulse, E. V. Lubenov, A. G. Siapas, Brain state dependence of hippocampal subthreshold activity in awake mice. *Cell Rep.* **18**, 136–147 (2017). doi: 10.1016/j.celrep.2016.11.084; pmid: 28052244
7. P. Rajasethupathy *et al*., Projections from neocortex mediate top-down control of memory retrieval. *Nature* **526**, 653–659 (2015). doi: 10.1038/nature15389; pmid: 26436451
8. K. Q. Shan, E. V. Lubenov, M. Papadopoulou, A. G. Siapas, Spatial tuning and brain state account for dorsal hippocampal CA1 activity in a non-spatial learning task. *eLife* **5**, e14321 (2016). doi: 10.7554/eLife.14321; pmid: 27487561
9. C. Xu *et al*., Distinct hippocampal pathways mediate dissociable roles of context in memory retrieval. *Cell* **167**, 961–972.e16 (2016). doi: 10.1016/j.cell.2016.09.051; pmid: 27773481
10. M. Kannan, G. Vasan, V. A. Pieribone, Optimizing strategies for developing genetically encoded voltage indicators. *Front. Cell. Neurosci.* **13**, 53 (2019). doi: 10.3389/fncel.2019.00053; pmid: 30863283
11. T. Knöpfel, C. Song, Optical voltage imaging in neurons: Moving from technology development to practical tool. *Nat. Rev. Neurosci.* **20**, 719–727 (2019). doi: 10.1038/s41583-019-0231-4; pmid: 31705060
12. H. H. Yang, F. St-Pierre, Genetically encoded voltage indicators: Opportunities and challenges. *J. Neurosci.* **36**, 9977–9989 (2016). doi: 10.1523/JNEUROSCI.1095-16.2016; pmid: 27683896
13. A. S. Abdelfattah *et al*., Bright and photostable chemigenetic indicators for extended in vivo voltage imaging. *Science* **365**, 699–704 (2019). doi: 10.1126/science.aav6416; pmid: 31371562
14. A. S. Abdelfattah *et al*., A general approach to engineer positive-going eFRET voltage indicators. *Nat. Commun.* **11**, 3444 (2020). doi: 10.1038/s41467-020-17322-1; pmid: 32651384
15. S. Chamberland *et al*., Fast two-photon imaging of subcellular voltage dynamics in neuronal tissue with genetically encoded indicators. *eLife* **6**, e25690 (2017). doi: 10.7554/eLife.25690; pmid: 28749338
16. L. Z. Fan *et al*., All-optical electrophysiology reveals the role of lateral inhibition in sensory processing in cortical layer 1. *Cell* **180**, 521–535.e18 (2020). doi: 10.1016/j.cell.2020.01.001; pmid: 31978320
17. Y. Gong *et al*., High-speed recording of neural spikes in awake mice and flies with a fluorescent voltage sensor. *Science* **350**, 1361–1366 (2015). doi: 10.1126/science.aab0810; pmid: 26586188
18. M. Kannan *et al*., Fast, in vivo voltage imaging using a red fluorescent indicator. *Nat. Methods* **15**, 1108–1116 (2018). doi: 10.1038/s41592-018-0188-7; pmid: 30420685
19. K. D. Piatkevich *et al*., A robotic multidimensional directed evolution approach applied to fluorescent voltage reporters. *Nat. Chem. Biol.* **14**, 352–360 (2018). doi: 10.1038/s41589-018-0004-9; pmid: 29483642
20. V. Villette *et al*., Ultrafast two-photon imaging of a high-gain voltage indicator in awake behaving mice. *Cell* **179**, 1590–1608.e23 (2019). doi: 10.1016/j.cell.2019.11.004; pmid: 31835034
21. H. H. Yang *et al*., Subcellular imaging of voltage and calcium signals reveals neural processing in vivo. *Cell* **166**, 245–257 (2016). doi: 10.1016/j.cell.2016.05.031; pmid: 27264607
22. Y. Adam *et al*., Voltage imaging and optogenetics reveal behaviour-dependent changes in hippocampal dynamics. *Nature* **569**, 413–417 (2019). doi: 10.1038/s41586-019-1166-7; pmid: 31043747
23. K. D. Piatkevich *et al*., Population imaging of neural activity in awake behaving mice. *Nature* **574**, 413–417 (2019). doi: 10.1038/s41586-019-1641-1; pmid: 31597963
24. S. Xiao *et al*., Large-scale voltage imaging in behaving mice using targeted illumination. *iScience* **24**, 103263 (2021). doi: 10.1016/j.isci.2021.103263; pmid: 34761183
25. Y. Gong, M. J. Wagner, J. Zhong Li, M. J. Schnitzer, Imaging neural spiking in brain tissue using FRET-opsin protein voltage sensors. *Nat. Commun.* **5**, 3674 (2014). doi: 10.1038/ncomms4674; pmid: 24755708
26. P. Zou *et al*., Bright and fast multicoloured voltage reporters via electrochromic FRET. *Nat. Commun.* **5**, 4625 (2014). doi: 10.1038/ncomms5625; pmid: 25118186
27. D. R. Hochbaum *et al*., All-optical electrophysiology in mammalian neurons using engineered microbial rhodopsins. *Nat. Methods* **11**, 825–833 (2014). doi: 10.1038/nmeth.3000; pmid: 24952910
28. N. C. Shaner *et al*., A bright monomeric green fluorescent protein derived from *Branchiostoma lanceolatum*. *Nat. Methods* **10**, 407–409 (2013). doi: 10.1038/nmeth.2413; pmid: 23524392
29. B. T. Bajar *et al*., Improving brightness and photostability of green and red fluorescent proteins for live cell imaging and FRET reporting. *Sci. Rep.* **6**, 20889 (2016). doi: 10.1038/srep20889; pmid: 26879144
30. J. Park *et al*., Screening fluorescent voltage indicators with spontaneously spiking HEK cells. *PLOS ONE* **8**, e85221 (2013). doi: 10.1371/journal.pone.0085221; pmid: 24391999
31. H. Zhang, E. Reichert, A. E. Cohen, Optical electrophysiology for probing function and pharmacology of voltage-gated ion channels. *eLife* **5**, e15202 (2016). doi: 10.7554/eLife.15202; pmid: 27215841
32. L. Stryer, Fluorescence energy transfer as a spectroscopic ruler. *Annu. Rev. Biochem.* **47**, 819–846 (1978). doi: 10.1146/annurev.bi.47.070178.004131; pmid: 354506
33. T. Kikukawa *et al*., Photochemistry of *Acetabularia* rhodopsin II from a marine plant, *Acetabularia acetabulum*. *Biochemistry* **50**, 8888–8898 (2011). doi: 10.1021/bi2009932; pmid: 21905737
34. T. Wada *et al*., Crystal structure of the eukaryotic light-driven proton-pumping rhodopsin, *Acetabularia* rhodopsin II, from marine alga. *J. Mol. Biol.* **411**, 986–998 (2011). doi: 10.1016/j.jmb.2011.06.028; pmid: 21726566
35. D. Maclaurin, V. Venkatachalam, H. Lee, A. E. Cohen, Mechanism of voltage-sensitive fluorescence in a microbial rhodopsin. *Proc. Natl. Acad. Sci. U.S.A.* **110**, 5939–5944 (2013). doi: 10.1073/pnas.1215595110; pmid: 23530193
36. L. Zimányi *et al*., Pathways of proton release in the bacteriorhodopsin photocycle. *Biochemistry* **31**, 8535–8543 (1992). doi: 10.1021/bi00151a022; pmid: 1327104
37. J. Platisa, G. Vasan, A. Yang, V. A. Pieribone, Directed evolution of key residues in fluorescent protein inverses the polarity of voltage sensitivity in the genetically encoded indicator ArcLight. *ACS Chem. Neurosci.* **8**, 513–523 (2017). doi: 10.1021/acschemneuro.6b00234; pmid: 28045247
38. B. A. Wilt, J. E. Fitzgerald, M. J. Schnitzer, Photon shot noise limits on optical detection of neuronal spikes and estimation of spike timing. *Biophys. J.* **104**, 51–62 (2013). doi: 10.1016/j.bpj.2012.07.058; pmid: 23332058
39. M. E. Garrett, I. Nauhaus, J. H. Marshel, E. M. Callaway, Topography and areal organization of mouse visual cortex. *J. Neurosci.* **34**, 12587–12600 (2014). doi: 10.1523/JNEUROSCI.1124-14.2014; pmid: 25209296
40. H. Taniguchi *et al*., A resource of Cre driver lines for genetic targeting of GABAergic neurons in cerebral cortex. *Neuron* **71**, 995–1013 (2011). doi: 10.1016/j.neuron.2011.07.026; pmid: 21943598
41. B. Tasic *et al*., Adult mouse cortical cell taxonomy revealed by single cell transcriptomics. *Nat. Neurosci.* **19**, 335–346 (2016). doi: 10.1038/nn.4216; pmid: 26727548
42. J. Zhuang *et al*., An extended retinotopic map of mouse cortex. *eLife* **6**, e18372 (2017). doi: 10.7554/eLife.18372; pmid: 28059700
43. S. T. Lim, D. E. Antonucci, R. H. Scannevin, J. S. Trimmer, A novel targeting signal for proximal clustering of the Kv2.1 $K^+$ channel in hippocampal neurons. *Neuron* **25**, 385–397 (2000). doi: 10.1016/S0896-6273(00)80902-2; pmid: 10719893
44. C. Cai *et al*., VolPy: Automated and scalable analysis pipelines for voltage imaging datasets. *PLOS Comput. Biol.* **17**, e1008806 (2021). doi: 10.1371/journal.pcbi.1008806; pmid: 33852574
45. H. Inan, M. A. Erdogdu, M. J. Schnitzer, "Robust estimation of neural signals in calcium imaging" in *NIPS'17: Proceedings of the 31st International Conference on Neural Information Processing Systems*, U. von Luxburg, I. Guyon, S. Bengio, H. Wallach, R. Fergus, S. V. N. Vishwanathan, R. Garnett, Eds. (Curran Associates Inc., 2017).
46. H. Inan *et al*., Fast and statistically robust cell extraction from large-scale neural calcium imaging datasets. bioRxiv 2021.2003.2024.436279 [Preprint] (2021); doi: 10.1101/2021.03.24.436279
47. E. Abs *et al*., Learning-related plasticity in dendrite-targeting layer 1 interneurons. *Neuron* **100**, 684–699.e6 (2018). doi: 10.1016/j.neuron.2018.09.001; pmid: 30269988
48. K. Cohen-Kashi Malina *et al*., NDNF interneurons in layer 1 gain-modulate whole cortical columns according to an animal's behavioral state. *Neuron* **109**, 2150–2164.e5 (2021). doi: 10.1016/j.neuron.2021.05.001; pmid: 34038743
49. M. He *et al*., Strategies and tools for combinatorial targeting of GABAergic neurons in mouse cerebral cortex. *Neuron* **92**, 555 (2016). doi: 10.1016/j.neuron.2016.10.009; pmid: 27764676
50. H. Adesnik, W. Bruns, H. Taniguchi, Z. J. Huang, M. Scanziani, A neural circuit for spatial summation in visual cortex. *Nature* **490**, 226–231 (2012). doi: 10.1038/nature11526; pmid: 23060193
51. L. Mesik *et al*., Functional response properties of VIP-expressing inhibitory neurons in mouse visual and auditory cortex. *Front. Neural Circuits* **9**, 22 (2015). doi: 10.3389/fncir.2015.00022; pmid: 26106301
52. J. Yu, H. Hu, A. Agmon, K. Svoboda, Recruitment of GABAergic interneurons in the barrel cortex during active tactile behavior. *Neuron* **104**, 412–427.e4 (2019). doi: 10.1016/j.neuron.2019.07.027; pmid: 31466734
53. M. Vinck, R. Batista-Brito, U. Knoblich, J. A. Cardin, Arousal and locomotion make distinct contributions to cortical activity patterns and visual encoding. *Neuron* **86**, 740–754 (2015). doi: 10.1016/j.neuron.2015.03.028; pmid: 25892300
54. J. Reimer *et al*., Pupil fluctuations track fast switching of cortical states during quiet wakefulness. *Neuron* **84**, 355–362 (2014). doi: 10.1016/j.neuron.2014.09.033; pmid: 25374359
55. C. K. Pfeffer, M. Xue, M. He, Z. J. Huang, M. Scanziani, Inhibition of inhibition in visual cortex: The logic of connections between molecularly distinct interneurons. *Nat. Neurosci.* **16**, 1068–1076 (2013). doi: 10.1038/nn.3446; pmid: 23817549
56. U. Knoblich, L. Huang, H. Zeng, L. Li, Neuronal cell-subtype specificity of neural synchronization in mouse primary visual cortex. *Nat. Commun.* **10**, 2533 (2019). doi: 10.1038/s41467-019-10498-1; pmid: 31182715
57. L. Cossell *et al*., Functional organization of excitatory synaptic strength in primary visual cortex. *Nature* **518**, 399–403 (2015). doi: 10.1038/nature14182; pmid: 25652823
58. J. Akerboom *et al*., Genetically encoded calcium indicators for multi-color neural activity imaging and combination with optogenetics. *Front. Mol. Neurosci.* **6**, 2 (2013). doi: 10.3389/fnmol.2013.00002; pmid: 23459413
59. H. Dana *et al*., Sensitive red protein calcium indicators for imaging neural activity. *eLife* **5**, e12727 (2016). doi: 10.7554/eLife.12727; pmid: 27011354
60. M. Inoue *et al*., Rational design of a high-affinity, fast, red calcium indicator R-CaMP2. *Nat. Methods* **12**, 64–70 (2015). doi: 10.1038/nmeth.3185; pmid: 25419959
61. M. Inoue *et al*., Rational engineering of XCaMPs, a multicolor GECI suite for in vivo imaging of complex brain circuit dynamics. *Cell* **177**, 1346–1360.e24 (2019). doi: 10.1016/j.cell.2019.04.007; pmid: 31080068
62. M. M. Karnani *et al*., Opening holes in the blanket of inhibition: Localized lateral disinhibition by VIP interneurons. *J. Neurosci.* **36**, 3471–3480 (2016). doi: 10.1523/JNEUROSCI.3646-15.2016; pmid: 27013676
63. W. Akemann *et al*., Imaging neural circuit dynamics with a voltage-sensitive fluorescent protein. *J. Neurophysiol.* **108**, 2323–2337 (2012). doi: 10.1152/jn.00452.2012; pmid: 22815406
64. F. Li *et al*., The connectome of the adult Drosophila mushroom body provides insights into function. *eLife* **9**, e62576 (2020). doi: 10.7554/eLife.62576; pmid: 33315010
65. J. Jackson, I. Ayzenshtat, M. M. Karnani, R. Yuste, VIP+ interneurons control neocortical activity across brain states. *J. Neurophysiol.* **115**, 3008–3017 (2016). doi: 10.1152/jn.01124.2015; pmid: 26961109
66. J. Reimer *et al*., Pupil fluctuations track rapid changes in adrenergic and cholinergic activity in cortex. *Nat. Commun.* **7**, 13289 (2016). doi: 10.1038/ncomms13289; pmid: 27824036
67. J. M. P. Pakan *et al*., Behavioral-state modulation of inhibition is context-dependent and cell type specific in mouse visual cortex. *eLife* **5**, e14985 (2016). doi: 10.7554/eLife.14985; pmid: 27552056
68. S. Xiao, H. A. Tseng, H. Gritton, X. Han, J. Mertz, Video-rate volumetric neuronal imaging using 3D targeted illumination. *Sci. Rep.* **8**, 7921 (2018). doi: 10.1038/s41598-018-26240-8; pmid: 29784920
69. M. L. Andermann *et al*., Chronic cellular imaging of entire cortical columns in awake mice using microprisms. *Neuron* **80**, 900–913 (2013). doi: 10.1016/j.neuron.2013.07.052; pmid: 24139817
70. J. C. Jung, A. D. Mehta, E. Aksay, R. Stepnoski, M. J. Schnitzer, In vivo mammalian brain imaging using one- and two-photon

fluorescence microendoscopy. *J. Neurophysiol.* **92**, 3121–3133 (2004). doi: 10.1152/jn.00234.2004; pmid: 15128753
71. R. P. Barretto, B. Messerschmidt, M. J. Schnitzer, In vivo fluorescence imaging with high-resolution microlenses. *Nat. Methods* **6**, 511–512 (2009). doi: 10.1038/nmeth.1339; pmid: 19525959
72. R. P. Barretto, M. J. Schnitzer, In vivo optical microendoscopy for imaging cells lying deep within live tissue. *Cold Spring Harb. Protoc.* **2012**, 1029–1034 (2012). doi: 10.1101/pdb.top071464; pmid: 23028071
73. Allen Institute for Brain Science, Cell types: Overview of the data, Allen cell types database; https://celltypes.brain-map.org/.
74. G. Buzsáki, C. A. Anastassiou, C. Koch, The origin of extracellular fields and currents—EEG, ECoG, LFP and spikes. *Nat. Rev. Neurosci.* **13**, 407–420 (2012). doi: 10.1038/nrn3241; pmid: 22595786
75. I. Soltesz, A. Losonczy, CA1 pyramidal cell diversity enabling parallel information processing in the hippocampus. *Nat. Neurosci.* **21**, 484–493 (2018). doi: 10.1038/s41593-018-0118-0; pmid: 29593317
76. L. Jin *et al*., Single action potentials and subthreshold electrical events imaged in neurons with a fluorescent protein voltage probe. *Neuron* **75**, 779–785 (2012). doi: 10.1016/j.neuron.2012.06.040; pmid: 22958819
77. C. Huang *et al*., Long-term optical brain imaging in live adult fruit flies. *Nat. Commun.* **9**, 872 (2018). doi: 10.1038/s41467-018-02873-1; pmid: 29491443
78. G. J. Goldey *et al*., Removable cranial windows for long-term imaging in awake mice. *Nat. Protoc.* **9**, 2515–2538 (2014). doi: 10.1038/nprot.2014.165; pmid: 25275789
79. P. Thévenaz, U. E. Ruttimann, M. Unser, A pyramid approach to subpixel registration based on intensity. *IEEE Trans. Image Process.* **7**, 27–41 (1998). doi: 10.1109/83.650848; pmid: 18267377
80. E. A. Pnevmatikakis, A. Giovannucci, NoRMCorre: An online algorithm for piecewise rigid motion correction of calcium imaging data. *J. Neurosci. Methods* **291**, 83–94 (2017). doi: 10.1016/j.jneumeth.2017.07.031; pmid: 28782629
81. K. He, G. Gkioxari, P. Dollar, R. Girshick, Mask R-CNN. *IEEE Trans. Pattern Anal. Mach. Intell.* **42**, 386–397 (2020). doi: 10.1109/TPAMI.2018.2844175; pmid: 29994331
82. F. Franke, R. Quian Quiroga, A. Hierlemann, K. Obermayer, Bayes optimal template matching for spike sorting - combining fisher discriminant analysis with optimal filtering. *J. Comput. Neurosci.* **38**, 439–459 (2015). doi: 10.1007/s10827-015-0547-7; pmid: 25652689
83. E. A. Pnevmatikakis *et al*., Simultaneous denoising, deconvolution, and demixing of calcium imaging data. *Neuron* **89**, 285–299 (2016). doi: 10.1016/j.neuron.2015.11.037; pmid: 26774160
84. E. A. Mukamel, A. Nimmerjahn, M. J. Schnitzer, Automated analysis of cellular signals from large-scale calcium imaging data. *Neuron* **63**, 747–760 (2009). doi: 10.1016/j.neuron.2009.08.009; pmid: 19778505
85. T. Deneux *et al*., Accurate spike estimation from noisy calcium signals for ultrafast three-dimensional imaging of large neuronal populations in vivo. *Nat. Commun.* **7**, 12190 (2016). doi: 10.1038/ncomms12190; pmid: 27432255
86. M. Kannan *et al*, Dual-polarity voltage imaging of the concurrent activation dynamics of multiple neuron types. Zenodo (2022); doi: 10.5281/zenodo.6361012

## ACKNOWLEDGMENTS

We thank Pierce scientific staff members C. Gardiner, M. Izydorsczak, P. O'Brien, X. Liu, T. Liu, and R. O'Brien for technical assistance; Pierce workshop members J. Buckley and A. Wilkins; G. Lur (University of California, Irvine) and K. Ferguson (Yale School of Medicine, New Haven) for advice on V1 imaging; and J. Verhagen (Yale Neuroscience) for comments on the manuscript. We further thank members of the Schnitzer laboratory: J. Li for animal husbandry and genotyping, Y. Zhang for virus handling and surgical advice, G. Delamare for instrumentation support, and F. Dinc and J. Li for computational consultations. All schematics were created using BioRender. **Funding:** This study was supported by NIH BRAIN Initiative grants U01NS103517 (V.A.P.), U01NS120822 (M.J.S. and G.V.), UF1NS107610 (M.J.S. and H. Zheng), and U19NS104590 (M.J.S. and I. Soltesz); and NSF NeuroNex grant DBI-1707261 (M.J.S. and K. Deisseroth). This research was funded in part by the Defense Advanced Research Projects Agency (DARPA) of the United States, contract nos. N6600117C4012 (NESD) and N6600119C4020 (N3) (V.A.P.). The views, opinions and/or findings expressed are those of the authors and should not be interpreted as representing the official views or policies of the Department of Defense or the US government. **Author contributions:** M.K. and G.V. conceived the project; designed, screened and characterized the sensors; and performed molecular biology and rAAV cloning. M.K. performed visual cortical surgeries. G.V. built the in vivo setup and wrote the software for V1 imaging. M.K. and G.V. conceived and performed in vivo V1 experiments and data analyses. S.H. conceived and performed the hippocampal experiments, wrote the SpikeImagingAnalysis pipeline, and performed data analyses for CA1 studies. C.H. performed and analyzed the fly experiments. R.C. built the optical setup used for CA1 imaging. J.L. designed the transgenic flies. J.A.C. shared the running wheel and provided advice on V1 imaging. M.K. and G.V. wrote the manuscript with contributions from all authors. M.J.S. developed data analyses, edited the manuscript, and supervised work at Stanford. V.A.P. supervised work at John B. Pierce and Yale. **Competing interests:** The authors declare no competing interests. **Data and materials availability:** All sequence information is available on GenBank (accession numbers OM687163 to OM687166 for soma-targeted Ace-mNeon2, pAce, VARNAM2, and pAceR, respectively). Plasmids and rAAVs will be made available through Addgene (help@addgene.org). Fly stocks have been deposited at the Bloomington Drosophila Stock Center, and all data and codes are available at Zenodo (*86*).  This research was funded in whole or in part by the Howard Hughes Medical Institute, a cOAlition S organization. The authors will make the Author Accepted Manuscript (AAM) version available under a CC BY public copyright license.

## SUPPLEMENTARY MATERIALS

science.org/doi/10.1126/science.abm8797
Figs. S1 to S26
Table S1
References (*87*, *88*)
MDAR Reproducibility Checklist

View/request a protocol for this paper from *Bio-protocol*.

Submitted 22 October 2021; accepted 3 October 2022
10.1126/science.abm8797

Science

# Dual-polarity voltage imaging of the concurrent dynamics of multiple neuron types

Madhuvanthi KannanGanesh VasanSimon HazizaCheng HuangRados#aw ChrapkiewiczJunjie LuoJessica A. CardinMark J. SchnitzerVincent A. Pieribone

*Science*, 378 (6619), eabm8797. • DOI: 10.1126/science.abm8797

**Real-time voltage imaging of neurons**

How different subpopulations of neurons coordinate their activity patterns in real time to control network output is still not fully understood. This is in part because of our inability to simultaneously measure the voltage dynamics within and across targeted cell ensembles. Kannan *et al*. developed a suite of mutually compatible, genetically encoded voltage indicators for high-speed voltage imaging of multiple genetically identified neurons in awake behaving animals. These indicators can be uniquely combined for simultaneous recordings of spiking by ensembles of neurons. This technical advance enables the first comprehensive studies of the real-time, millisecond-scale interactions between neurons of distinct genetic classes. —PRS







*Science* (ISSN ) is published by the American Association for the Advancement of Science. 1200 New York Avenue NW, Washington, DC 20005. The title *Science* is a registered trademark of AAAS.